André Simões Praça

Licenciado em Ciências da Engenharia Mecânica

Predictive analytical and numerical modeling for orthogonal cutting

Dissertação para obtenção do Grau de Mestre em
Engenharia Mecânica

Orientador: Professor Doutor Jorge Joaquim Pamies
Teixeira, FCT-UNL

Júri:

Presidente: Prof. Doutor José Fernando de Almeida Dias
Arguente: Prof. Doutora Carla Maria Moreira Machado
Vogal: Prof. Doutor Jorge Joaquim Pamies Teixeira

FACULDADE DE
CIÊNCIAS E TECNOLOGIA
UNIVERSIDADE NOVA DE LISBOA

Setembro de 2014

LOMBADA

Predictive analytical and numerical modeling for orthogonal cutting

André Simões Praça

2014

André Simões Praça

Licenciado em Ciências da Engenharia Mecânica

Predictive analytical and numerical modeling for orthogonal cutting

Dissertação para obtenção do Grau de Mestre em
Engenharia Mecânica

Orientador: Professor Doutor Jorge Joaquim Pamies
Teixeira, FCT-UNL

Júri:

Presidente: Prof. Doutor José Fernando de Almeida Dias
Arguente: Prof. Doutora Carla Maria Moreira Machado
Vogal: Prof. Doutor Jorge Joaquim Pamies Teixeira

FACULDADE DE
CIÊNCIAS E TECNOLOGIA
UNIVERSIDADE NOVA DE LISBOA

Setembro de 2014

Copyright

Predictive analytical and numerical modeling for orthogonal cutting

Faculdade de Ciências e Tecnologia da Universidade Nova de Lisboa

Acknowledgements

First and foremost I’d like to thank my advisor, Professor Jorge Joaquim Pamies Teixeira, for offering me the opportunity to work in a challenging field of research, and believing I was the person for it. I’d also like to thank him for being open to the idea of seeing where it would lead, for the general support and knowledge, by making it interesting, and helping me see the bigger picture when in the midst of it all.

I’d like to thank my parents, to whom I dedicate this work, for always believing in me and the patience for the days when not all went well. To my father for always pushing me to do more and do better, to my mother for the constant reminder that I can do anything I set my mind to because if others have done it, so can I. This work, and everything I will ever achieve of importance, is theirs.

I’d also like to thank two people who, not only during this work, but also during my entire academic journey have contributed to making it as fun as possible, and helped me overcome every academic obstacle, António Figueiredo and Bruno Palma (in no specific order).

Finally, I’d like to thank the people who during this work have supported me whether with just a word or two like “you can do it”, or with a daily dose of “is it done yet?”.

Agradecimentos

Em primeiro lugar gostaria de agradecer ao meu orientador, Professor Jorge Joaquim Pamies Teixeira, por me ter dado a oportunidade de trabalhar num campo de pesquisa desafiante, e ter acreditado que eu era a pessoa para o fazer. Também gostaria de lhe agradecer por ter estado aberto à ideia de ver onde ele nos levaria, pelo apoio e conhecimento, por tê-lo tornado interessante, e por me ter ajudado a ver o quadro geral quando eu ficava preso em detalhes.

Gostaria de agradecer aos meus pais, a quem dedico este trabalho, por sempre terem acreditado em mim e pela paciência nos dias em que nem tudo corria bem. Ao meu pai por sempre me impulsionar a fazer mais e melhor, à minha mãe por me recordar constantemente que eu consigo fazer tudo aquilo que penso em fazer, visto que se outros o conseguem, então eu também consigo. Este trabalho, e tudo o que eu alguma vez alcançar de importante, são deles.

Também gostaria de agradecer a duas pessoas que, não apenas durante a duração deste trabalho, mas também durante a minha jornada académica, a tornaram divertida e me terem ajudaram a ultrapassar cada obstáculo académico, António Figueiredo e Bruno Palma (em nenhuma ordem específica).

Finalmente, gostaria também de agradecer às pessoas que durante este trabalho me apoiaram, fosse apenas com uma palavra ou duas, tais como, “tu consegues”, ou com uma dose diária de “isso já está?”.

ABSTRACT

In this thesis, a predictive analytical and numerical modeling approach for the orthogonal cutting process is proposed to calculate temperature distributions and subsequently, forces and stress distributions. The models proposed include a constitutive model for the material being cut based on the work of Weber, a model for the shear plane based on Merchants model, a model describing the contribution of friction based on Zorev's approach, a model for the effect of wear on the tool based on the work of Waldorf, and a thermal model based on the works of Komanduri and Hou, with a fraction heat partition for a non-uniform distribution of the heat in the interfaces, but extended to encompass a set of contributions to the global temperature rise of chip, tool and work piece.

The models proposed in this work, try to avoid from experimental based values or expressions, and simplifying assumptions or suppositions, as much as possible. On a thermo-physical point of view, the results were affected not only by the mechanical or cutting parameters chosen, but also by their coupling effects, instead of the simplifying way of modeling which is to contemplate only the direct effect of the variation of a parameter. The implementation of these models was performed using the MATLAB environment.

Since it was possible to find in the literature all the parameters for AISI 1045 and AISI O2, these materials were used to run the simulations in order to avoid arbitrary assumption.

Key terms:

Orthogonal cutting, cutting temperature modeling, thermal model, non-uniform heat intensity, temperature distributions.

RESUMO

Nesta dissertação, é proposta uma abordagem de modelação analítica e numérica da previsão do processo de corte ortogonal, para o cálculo das distribuições de temperatura, e subsequentemente das distribuições de forças e tensões. Os modelos propostos incluem um modelo constitutivo do material a ser cortado baseado no trabalho de Weber, um modelo para o plano de corte baseado no modelo de Merchant, um modelo que descreve a contribuição do atrito baseado na abordagem de Zorev, um modelo para o efeito do desgaste na ferramenta baseado no trabalho de Waldorf, e um modelo térmico baseado nos trabalhos de Komanduri e Hou, com uma fracção de partilha de calor para uma distribuição disforme do calor nas interfaces, mas estendido de forma a englobar um conjunto de contribuições para a subida global de temperatura da apara, ferramenta e peça. Trata-se pois de uma síntese de vários estudos que contribui para o alargamento do conhecimento científico neste domínio.

Os modelos propostos neste trabalho, tentam evitar valores ou expressões obtidas experimentalmente, e simplificações ou suposições, o máximo possível. Do ponto de vista termofísico, os resultados foram afectados não apenas pelos parâmetros mecânicos ou de corte escolhidos, mas também pela correlação dos efeitos, em vez da maneira simplista de modelação onde apenas são contemplados os efeitos directos da variação de um parâmetro. A simulação dos modelos criados foi realizada através da sua programação na plataforma MATLAB.

Para evitar suposições e simplificações arbitrárias utilizaram-se os aços AISI 1045 e o AISI O2, uma vez que na literatura foram encontrados os dados necessários para a modelação destes materiais.

Termos-chave:

Corte ortogonal, modelação de temperaturas de corte, método da fonte de calor, intensidade não-uniforme do calor, distribuições de temperatura.

Contents

LIST OF FIGURES

LIST OF TABLES

SIMBOLS

σ^*	Thermal part of the elastic-viscoplastic model
σ^*_0	Yield stress at 0 ºK
m, n	Related to the shape of obstacles
$T_{dislocations}$	Temperature at which the dislocations overcome obstacles
ΔG_0	Free activation enthalpy
k_B	Boltzmann constant
$\dot{\bar{\varepsilon}}_p$	Equivalent plastic strain rate
$\dot{\varepsilon}_0$	Critical strain rate
σ_G	Athermal part of the elastic-viscoplastic model
σ_{G_0}	Initial athermal flow stress
k	Hardening coefficient
r	Strain hardening exponent
$\bar{\varepsilon}_p$	Equivalent plastic strain
G	Shear modulus
E	Young’s modulus
ν	Poisson ratio
e_1, e_2	Experimentally determined to calculate E
$\Delta\nu$	Experimentally determined to calculate ν
$g(T, T_t)$	Describes the softening of the material at high temperature
ξ, ζ	Used to adjust the slope of the flow stress decrease
T_{melt}	Melting temperature of the material
T_t	Transition temperature
ϑ_0, $\Delta\vartheta$	Used to adjust to specific material

V_C	Cutting speed
V_{Chip}	Chip velocity
V_S	Velocity across the shear plane
V_N	Normal component of V_C
γ_{AB}	Shear strain on the material crossing the shear plane
R	Resultant force
F_N	Normal force at the shear plane
F_S	Shear force at the shear plane
F_{Frict}	Frictional on the tool-chip interface force
F_{Normal}	Normal to the tool-chip interface force
α	Rake angle
λ	Friction angle
Φ	Shear angle
θ	Useful angle
$\dot{\gamma}_{AB}$	Shear strain-rate of the material crossing the shear plane
C	Shear strain rate constant
l	Length of the shear plane
t_1	Undeformed chip thickness
ε_{AB}	Strain on the material crossing the shear plane
$\dot{\varepsilon}_{AB}$	Strain rate on the material crossing the shear plane
τ_S	Shear stress of the material
τ_C	Shear yield stress of the material
$\tau_{friction}$	Shear stress on the rake face
μ_{local}	Local friction coefficient
P	Normal pressure
P_0	Normal stress exerted on the rake face at the tool tip
ψ	Exponential constant representing the distribution of the pressure

l_C	Length of contact in chip-tool interface
l_p	Length of the sticking zone in chip-tool interface
τ_{wear}	Stress distributions under the flank wear area
μ	Friction coefficient
q	Heat liberation intensity of the heat source
a_c	Thermal diffusivity of chip material
λ_c	Thermal conductivity of chip material
λ_t	Thermal conductivity of tool material
K_0	Bessel function of the second kind and zero order
T_M	Temperature rise at point M
$T_{shear\ chip}$	Temperature rise in the chip due to the shear heat source
q_{shear}	Heat liberation intensity of the heat source in the shear zone
$T_{friction\ chip}$	Temperature rise in the chip due to the friction heat source
$q_{friction}$	Heat liberation intensity of the friction heat source
B_{chip}	Heat partition fraction between the chip and the tool, chip side
$\tau_{friction}$	Friction stress along the rake face
W	Width of cut
$T_{shear\ work}$	Temperature rise in the work piece due to the shear heat source
$T_{friction\ tool}$	Temperature rise in the tool due to the friction heat source
B_{tool}	Heat partition fraction between the chip and the tool, tool side
$T_{induction\ on\ rake\ tool}$	Temperature rise in the tool due to induction on rake heat source
$q_{induction\ on\ rake}$	Induction on rake heat liberation intensity
$B_{induction\ rake}$	Heat partition fraction for induction of the shear heat source
$T_{rubbing\ work}$	Temperature rise in the work piece due to the rubbing heat source
$q_{rubbing}$	Heat liberation intensity of the rubbing heat source
l_{fc}	Length of the wear flank

B_f	Heat partition fraction between work piece and the tool, work side
$T_{rubbing\ work}$	Temperature rise in the work piece due to the rubbing heat source
$T_{rubbing\ tool}$	Temperature rise in the tool due to the rubbing heat source
$T_{induction\ on\ flank\ tool}$	Temperature rise in the tool due to induction on flank heat source
$q_{induction\ on\ flank}$	Induction on flank heat liberation intensity
T_{amb}	Ambient temperature
$\Delta\mathbf{B}_i$, m_i, C_i, k_i	Heat partition ratio

1

INTRODUCTION

This chapter presents the motivation and objectives as well as the structure of this thesis.

1.1. Motivation

The production industry today needs to be able to produce as much as possible in limited time, and optimizing its processes is usually a main goal. When the metal cutting process is considered, the cutting tool life is an important aspect to improve for an optimized process. This aspect is influenced by how much accuracy the tool needs to maintain and how fast it wears to an unacceptable point. In this industry world, the tool life is usually estimated by means of empirical formulas, past experiences, or directives from the tool producer. But if the goal was to develop and better understand the cutting process in order to create an even more optimized process, then a predictive model with its basis on the fundamental thermo-mechanical knowledge, with as little empirical data as possible, would be useful.

The search for this type of model was the motivation for this thesis, specifically a model which predicts the temperature rise, not only on the chip, but also on the tool and work piece, since temperature rise has a very influential contribution to the tool wear.

On the other hand, in order to decrease the temperature rise in the cutting process cooling liquids are used, but since European norms point to the elimination of these chemical products of the production process, a good understanding of the temperature rise process may also help to decrease temperature rise without those liquids.

Finally, the nature of the cutting process restricts a good experimental measurement of the temperatures in the tool, if the mean values of temperature are not the actual goal, this model may also help research on the areas where the highest actual temperature point is the question.

1.2. Objectives

The main objectives of this thesis were to better understand the fundamentals of the thermo-mechanical process involved in orthogonal metal cutting, the analytical models proposed so far in temperature prediction during that process, and to create a numerical model compiling those analytical models to create an overall more extended or comprehensive model that is not only sensitive to different parameters (mechanical and thermo-mechanical) and their coupling effects, but also encompasses all the different contributions to the temperature rises and can be used as groundwork for future investigation in this area.

1.3. Document structure

This document is divided into five chapters.

In chapter 1 the theme of this thesis is introduced and the motivation, objectives and structure are presented.

In chapter 2 the subjects relevant to this thesis are discussed, it is described what was done before, also known as the state-of-the-art, which is divided into six types of models relevant to the thermo-mechanical modeling of orthogonal cutting.

In chapter 3 the analytical and numerical models adopted in this work for predicting the temperature rise in orthogonal cutting are presented, and is divided into four parts corresponding to the different temperature models.

In chapter 4 the results of this investigation are reported and discussed, and is divided into five parts corresponding to the different temperatures calculated with the models.

Finally, in chapter 5 the main conclusions resulting from this work are presented and suggestions for future work are proposed.

2

STATE-OF-THE-ART

This chapter presents the relevant subjects to this thesis. Introduces fundamental concepts and refers studies by the most relevant authors.

2.1. Thermo-mechanical modeling of orthogonal cutting

The modeling of the thermo-mechanical aspects in metal cutting is a complex subject which involves several components and coupling effects, nevertheless the process can be divided into various types of models for a better and deeper understanding.

2.1.1. Constitutive model for the workpiece material

The success and reliability of modeling depends upon accurate mechanical (elastic constants, flow stress, friction, fracture stress/strain, etc.) and thermo-physical (density, thermal conductivity, heat capacity, etc.) data. A realistic material model should also include strain-hardening and thermal softening due to dynamic recovery or recrystallization [1].

Oxley [2] observed that only superficial consideration could be given in analyses based on models with constant flow stress, which could account for the poor agreement between predicted and experimental results. He also added that only with a model with variable flow stress due to strain, strain rate and temperature could the importance of speed and size effects in machining be explained. His model expressed flow stress as work-hardening behavior and has been used in slip-line modeling of low and medium carbon steels.

A well accepted material model is the Johnson-Cook constitutive model, for modeling and simulation studies, since it takes into account strain and strain-rate hardening, as well as thermal softening of the material while being numerically robust [3]. The main problem is that it does not take into account the coupling effect of strain and strain-rate, strain and temperature or strain rate and temperature.

Sima and Özel [4] did not consider a damage or material failure model, taking into account that serration (crack initiation mechanism in the primary shearing zone) is caused by adiabatic shearing due to temperature-dependent flow softening, for this they used Calamaz model. This model introduced modifications on the Johnson-Cook model such as a flow softening at elevated strains and temperatures (showing a decreased behavior in flow stress with increased strain beyond a critical strain value, but still exhibiting strain hardening below that value).

Weber *et al*. [5], provided an elastic-viscoplastic behavior of the material by developing a model that consists of two parts, one thermal and the other athermal. In order to express the flow stress as a function of temperature, the proposed model assumes that dislocations slips are thermally activated. At low temperatures they are affected by short range small obstacles and are basically independent of the strain rate (typical behavior of BCC metals). However, for higher temperatures, dislocations can overcome obstacles without additional stress. Thus the thermal part is expressed by:

$$\sigma^* = \sigma_0^* \cdot \left(1 - \left(\frac{T}{T_{dislocations}}\right)^n\right)^m \tag{2.1}$$

where σ^*_0 represents the yield stress at 0 K, m and n are related to the shape of obstacles and $T_{dislocations}$ is the temperature at which the dislocations can overcome those obstacles. This temperature can be calculated from the free activation enthalpy ΔG_0 necessary to overcome the decisive obstacles using the following equation:

$$T_{dislocations} = \frac{\Delta G_0}{k_B \cdot \ln\left(\frac{\dot{\varepsilon}_0}{\dot{\bar{\varepsilon}}_p}\right)} \tag{2.2}$$

where k_B is the Boltzmann constant, $\dot{\bar{\varepsilon}}_p$ is the equivalent plastic strain rate and $\dot{\varepsilon}_0$ the critical strain rate necessary to move the dislocations. The model introduces an athermal contribution to describe the reduction of mobility of the dislocations and a strain-hardening effect of the global material flow stress due to the microstructures configuration (dislocations, grain boundaries, precipitations and solute atoms). This contribution is expressed by:

$$\sigma_G = (\sigma_{G_0} + k \cdot \bar{\varepsilon}_p^r) \cdot \frac{G(T)}{G(0K)} \cdot g(T, T_t) \tag{2.3}$$

where σ_{G_0} is the initial athermal flow stress, k is the hardening coefficient, r the strain hardening exponent and $\bar{\varepsilon}_p$ is the equivalent plastic strain. Although the athermal contribution does not depend directly on the temperature, it depends on the shear modulus G, Young's modulus E and the Poisson ratio ν, which vary with temperature, as follows:

$$\begin{cases} G(T) = \dfrac{E(T)}{2[1 + \nu(T)]} \\ E(T) = E(273K) + e_1(T - 273K) + e_2(T - 273K)^2 \\ \nu(T) = \nu(273K) + \Delta\nu(T - 273K) \end{cases} \tag{2.4}$$

Parameters e_1 e_2, and $\Delta\nu$ are experimentally determined. The $g(T, T_t)$ function in eq. (2.3) describes the softening of the material at high temperature (above the transition temperature) and can be expressed by:

$$g(T, T_t) = \begin{cases} 1 & for\ T \le T_t \\ \left(1 - \left(\dfrac{T - T_t(\dot{\bar{\varepsilon}}_p)}{T_{melt} - T_t(\dot{\bar{\varepsilon}}_p)}\right)^\xi\right)^\zeta & for\ T > T_t \end{cases} \tag{2.5}$$

The parameters ξ and ζ are used to adjust the slope of the flow stress decrease and T_{melt} denotes the melting temperature of the material. In turn, the transition temperature is given by:

$$T_t(\dot{\bar{\varepsilon}}_p) = \vartheta_0 + \Delta\vartheta \cdot \ln\left(1 + \frac{\dot{\bar{\varepsilon}}_p}{\dot{\varepsilon}_0}\right) \tag{2.6}$$

showing its dependency on the equivalent plastic strain rate and the critical strain rate. Parameters ϑ_0 and $\Delta\vartheta$ are used to adjust to specific material in use.

In conclusion the constitutive material model is given by,

$$\sigma = \sigma_0^* \cdot \left(1 - \left(\frac{T}{T_{dislocations}}\right)^n\right)^m + (\sigma_{G_0} + k \cdot \bar{\varepsilon}_p^r) \cdot \frac{G(T)}{G(0K)} \cdot g(T, T_t) \tag{2.7}$$

2.1.2. **Shear plane model**

One of the most basic characteristics of machining processes lies in its extremely complicated flow of chip material taking place over the whole range of the “shear deformation zone”. It can be said that the characteristics of machining processes can be well understood so long as the rules of the flow of the chip material are known. These rules not only come from the mechanical but also the kinematic aspects. An acceptable model for machining must simultaneously satisfy both stress equilibrium and velocity (volume constancy) requirements of the flow of the chip material [6].

This particular case in study is where the cutting edge of the tool is arranged to be perpendicular to the direction of relative work-tool motion, because it represents a two-dimensional rather than a three-dimensional problem (eliminating several independent variables). This is widely used in theoretical and experimental work and is known as orthogonal cutting (figure 2.1) [7].

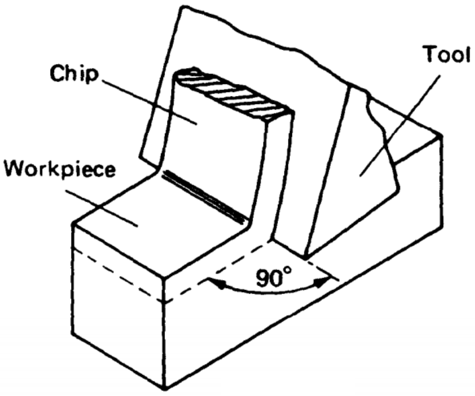

Figure 2.1 – Orthogonal cutting [7].

The basic metal orthogonal cutting process has been accepted by many modern theories to be close to the one proposed by Mallock more than 100 years ago (figure 2.2a), although there has been backward steps (for some years there was a misconception that the process could be likened to the splitting of wood where a crack occurred ahead of the tool (figure 2.2b)), the conceptual outline has remained fairly similar, like in the well-known and fundamental work of Ernst and Merchant on the mechanics of the process [7].

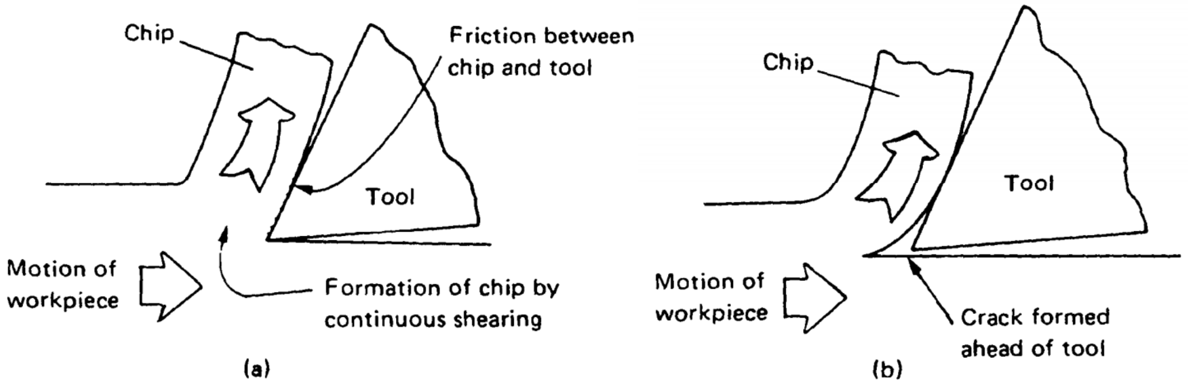

Figure 2.2 - Models of cutting process. a) Accepted model; b) earlier misconception [7].

This accepted model is based on a continuous chip being formed by plastic deformation in a narrow zone that runs from the tool cutting edge to the work-chip free surface, represented by a shear plane (from A to B) across which V_C, the cutting speed, is instantaneously changed to V_{Chip}, the chip velocity, assuming the tool is stationary, this requires a discontinuity in the tangential component of velocity, across the shear plane equal to V_S as shown by the velocity diagram (figure 2.3).

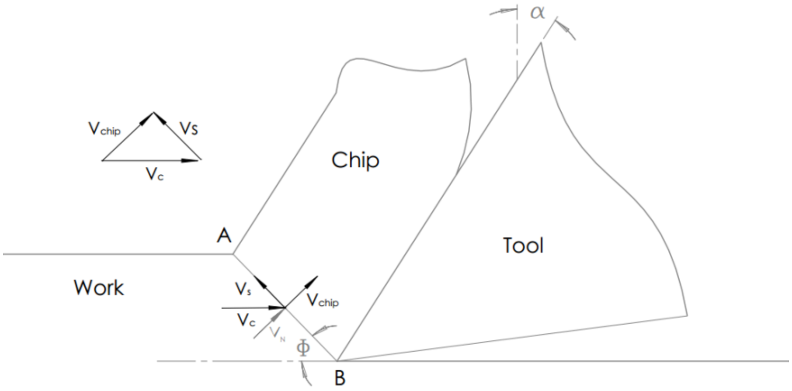

Figure 2.3 – Shear plane model: Velocity diagram.

From this diagram the velocities described can be expressed by the relationships:

$$V_{chip} = \frac{\sin \Phi}{\cos(\Phi - \alpha)} \cdot V_c \tag{2.8}$$

$$V_s = \frac{\cos \alpha}{\cos(\Phi - \alpha)} \cdot V_c \tag{2.9}$$

$$V_N = \sin \Phi \cdot V_c \tag{2.10}$$

Where V_C is usually known and V_N is the normal component of V_C to the shear plane.

The model, as described, is only valid for an idealized rigid-perfectly plastic (non-workhardening) material, disregarding elastic strain and the variation of volume of the elements in the material. And so, for the conservation of mass to occur, the normal component of velocity must be continuous across the shear plane, which implies that the normal to the shear plane component of the cutting speed (V_N)

and chip velocity (V_{chip}) must be equal. This shear plane as a plane of tangential velocity discontinuity is the direction of maximum shear strain rate and, due to the isotropic plasticity theory, the direction of maximum shear stress. The shear strain occurring in crossing a tangential velocity discontinuity is given by the magnitude of the discontinuity divided by the magnitude of the component of velocity normal to the discontinuity. Hence the shear strain on the material crossing the shear plane, γ_{AB}, using equations (2.9) and (2.10), can be given by:

$$\gamma_{AB} = \frac{V_S}{V_N} = \frac{\cos\alpha}{\sin\Phi \cdot \cos(\Phi - \alpha)} \tag{2.11}$$

However when considering material hardening during deformation, the discontinuity in the tangential component of velocity is no longer acceptable, leading to the shear plane becoming a shear zone. Nevertheless, when the shear plane is considered straight, as in most shear plane theories, and the tool is perfectly sharp, the mean compressive (hydrostatic) stress is constant along the plane and the resultant force, R, passes through its mid-point and is transmitted entirely to the tool-chip interface (along the rake face of the tool where the chip is in contact). In the case where the tool has a wear flank the resultant force is expected to move in the shear plane to a point near the tool tip. These resultant forces can be decomposed into a set of components as shown in the diagram of forces (figure 2.4).

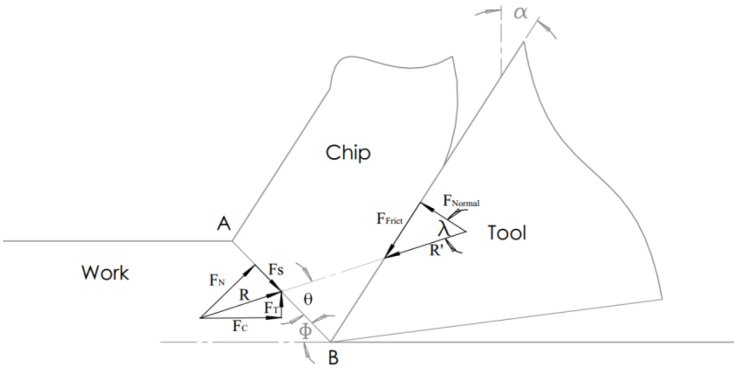

Figure 2.4 – Shear plane model: Forces diagram.

Where R can be decomposed into a force in the cutting direction and normal to this direction, F_C and F_T, or into F_N and F_S, a normal and shear force at the shear plane. The opposed resultant force, R', can be decomposed into a frictional and a normal to the tool-chip interface force, F_{Frict} and F_{Normal}. Later in this document will be shown how to know the value of some forces, and with the relationships in the forces diagram all the other forces can be known.

For the shear model to be completely defined all that is left is to know the angles, and while α is a constant of the tool (rake angle), λ and Φ are a source of several scientific studies and many proposed theories.

2.1.3. **Shear plane solutions**

Despite earlier attempts by Piispanen, the first complete analysis resulting in a solution for the shear angle, Φ, was presented by Ernst and Merchant. In their analysis the chip is assumed to behave as a rigid body held in equilibrium by the action of forces transmitted across the chip-tool interface (as seen in figure 2.4), but the basis of Ernst and Merchant's theory was the suggestion that the shear angle would take such a value as to maximize the shear stress in the shear plane. With this assumption, Merchant considered Φ to be given by:

$$\Phi_M = \frac{\pi}{4} + \frac{\alpha - \lambda}{2} \tag{2.12}$$

Where the friction angle, λ, is given by;

$$\mu = \tan\ (\lambda) \tag{2.13}$$

And μ is a known friction coefficient.

Oxley developed an analytical model known as the parallel-sided shear zone theory (figure 2.5).

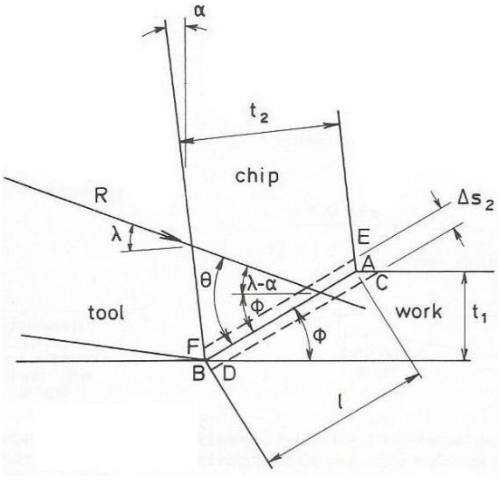

Figure 2.5 – Parallel-sided shear zone model [2].

In this theory, the overall geometry of the shear zone model is the same as for the shear plane model (figure 2.3) with AB and Φ geometrically equivalent to the shear plane and shear angle (enabling the use of equation (2.12) for its calculation). The shear plane AB of the shear model is assumed to be open to two boundaries, one between the shear plane and the workpiece (CD in figure 2.5) and the other between the shear plane and the chip (EF in figure 2.5), both parallel and equidistant from the shear plane. The cutting velocity is assumed to change to the chip velocity in the shear zone along smooth geometrical identical streamlines with no discontinuities in velocity. The velocity (figure 2.3) and force (figure 2.4) geometry and its relationships remain the same, although the resultant force, R, will not in general pass through the midpoint of AB.

The methodology used in this theory, consists of the determination of the stresses along AB, in terms of Φ and the work material properties and, from these, the magnitude and direction of the resultant force R transmitted by AB, assuming the tool to be perfectly sharp, Φ is then chosen so that the resultant force is consistent with the frictional conditions at the tool-chip interface. From the assumptions made the shear strain will be constant along AB as will the shear strains along CD and EF [2], where the shear strain along EF is given by:

$$\gamma_{EF} = \frac{V_S}{V_N} = \frac{\cos\alpha}{\sin\Phi \cdot \cos(\Phi - \alpha)} \tag{2.14}$$

Because half of this strain occurs at AB, γ_{AB} is now given by:

$$\gamma_{AB} = \frac{\cos\alpha}{2 \cdot \sin\Phi \cdot \cos(\Phi - \alpha)} \tag{2.15}$$

The shear strain-rate, also constant along AB, is given by:

$$\dot{\gamma}_{AB} = C \cdot \frac{V_S}{l} \tag{2.16}$$

Where C is a shear strain rate constant and l is the length of the shear plane, obtained geometrically from the undeformed chip thickness, t_1:

$$l = \frac{t_1}{\sin\Phi} \tag{2.17}$$

With the shear strain and the shear strain rate now known, the strain and strain rate can be easily obtained, using the von Mises criterion, by:

$$\varepsilon_{AB} = \frac{\gamma_{AB}}{\sqrt{3}} \tag{2.18}$$

$$\dot{\varepsilon}_{AB} = \frac{\dot{\gamma}_{AB}}{\sqrt{3}} \tag{2.19}$$

Also due to von Mises criterion, the shear stress, τ_S, with the normal stress determined by the equation (2.7) along the shear plane AB, is given by:

$$\tau_S = \frac{\sigma_{AB}}{\sqrt{3}} \tag{2.20}$$

Determined in the same way but considering the equivalent plastic strain to be zero, the shear yield stress of the material τ_C is given by:

$$\tau_C = \frac{\sigma_c}{\sqrt{3}} \tag{2.21}$$

And finally the useful angle θ (see figure 2.5) is given by:

$$\tan\theta = 1 + 2\left(\frac{\pi}{4} - \Phi\right) - C \cdot r \tag{2.22}$$

Where r is the same value used in equation (2.3) and can be called a strain-hardening index [2].

Lee and Shaffer (figure 2.6a), attempted to apply the plasticity theory to the problem of orthogonal metal cutting with the mathematical foundations for constructing slip-lines from Hill [8]. Many researchers pursued the slip-lines way of thought, notable among these include the centered-fan slip-line model for machining with restricted contact tools by Johnson, Usui and Hoshi (figure 2.6b); Kudo’s admissible and inadmissible slip-line models for machining (figure 2.6c); Dewhurst’s slip-line solutions for non-unique machining with curled chip formation (figure 2.6d); and the subsequent extended curled chip formation model by Shi and Ramalingam (figure 2.6e). Later, Fang, Jawahir and Oxley developed a universal slip-line model that incorporates some of the previously referred slip-line models (figure 2.6f) [6].

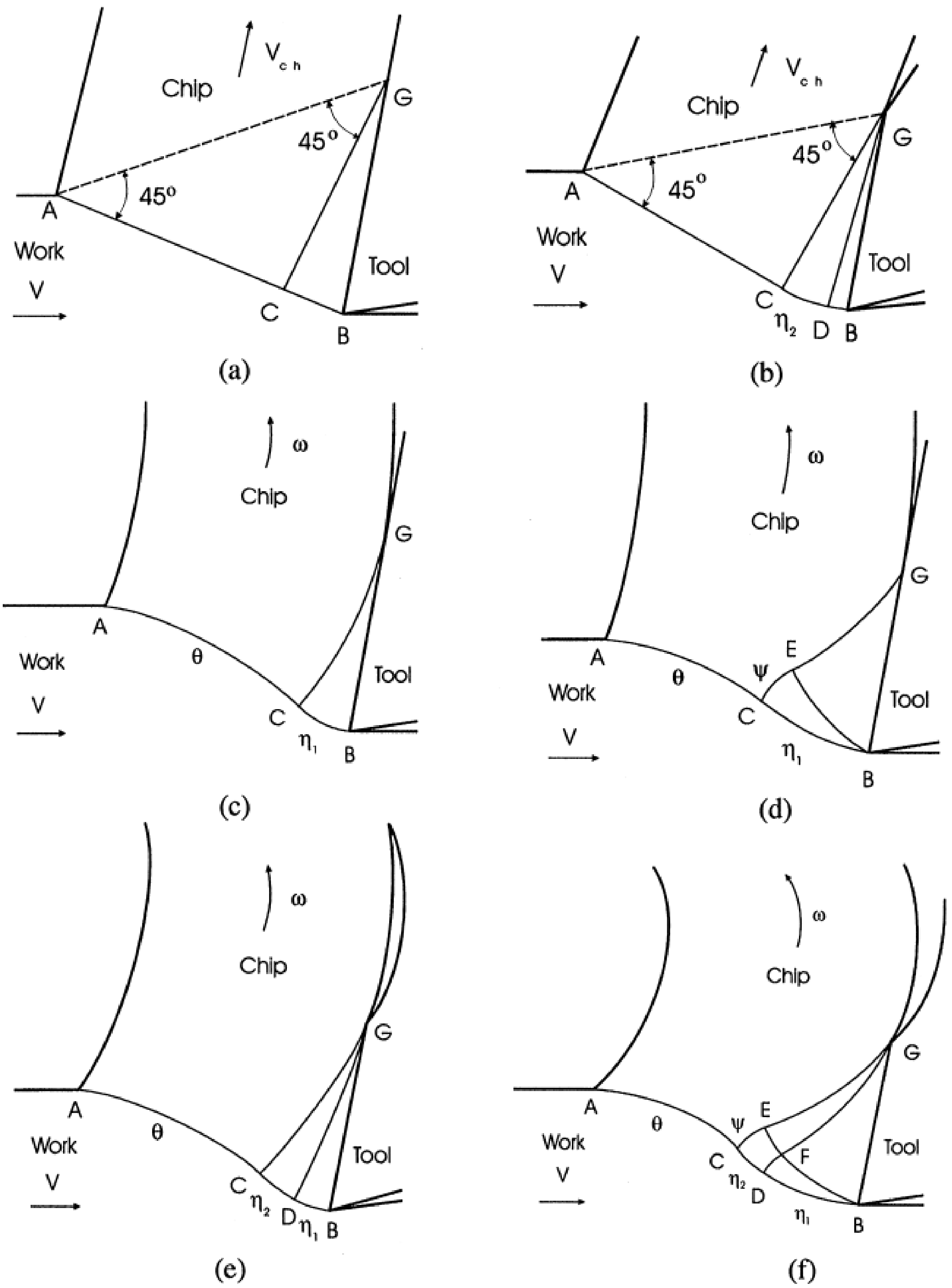

Figure 2.6 – a) Lee and Shaffer’s model; b)Johnson’s, Usui and Hoshi’s model; c)Kudo’s model; d) Dewhurst’s model; e) Shi and Ramalingam’s model; and f) Fang, Jawahir and Oxley’s model. (Adapted from [6]).

These physics-based analytical methods developed over decades provide a strong foundation for quantitative modeling of machining processes, subsequently promoting interest in numerical modeling (e.g., the Finite Element Modeling and others) [8].

2.1.4. **Friction model**

Since a large part of the cutting force required in machining is transmitted to the work material through the rake face of the tool, it is important to understand the stress distribution acting along the tool rake face in machining of engineering materials in order to consider the mechanisms of chip deformation and the relationship between chip deformation and characteristics of material, and also to understand the conditions of contact at that interface [9, 10].

Earlier models of metal cutting ignored friction conditions at the chip-tool interface or assumed them to be constant with a coefficient of friction based on Coulomb’s law. In the Merchant’s model, that friction coefficient comes from a mean apparent or global coefficient friction value, which can be estimated from the experimental values of cutting forces. Oxley’s model suggests that the tool-chip contact is perfectly sticking with internal shearing of work material within the chip [11].

Eventually, Zorev approached the problem by proposing distribution forms for the normal pressure and shear stress distribution. He proposed that the material exiting the shear zone reaches the rake face with such a high normal pressure that there is a sticking contact zone close to the tool tip in a plastic contact condition, then due to the drop in the normal pressure the contact state changes to the sliding (Coulomb) friction, away from the tool tip on the rake face in an elastic contact condition (figure 2.7) [10].

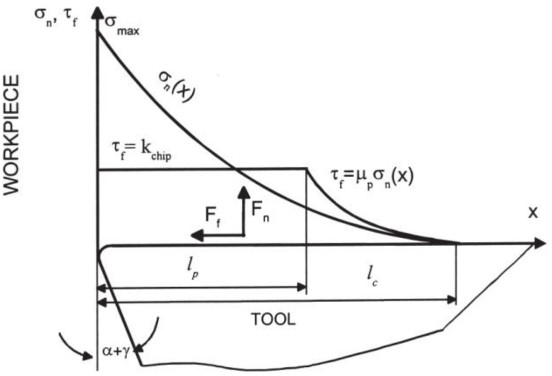

Figure 2.7 - Curves representing normal and frictional stress distributions on the tool rake face [12]

This behavior was verified by experimental researches in later studies, some with a split-tool measuring the normal pressure and shear stress distributions on the rake face [9].

It can be observed from the figure 2.7, that the shear stress on the rake face is equal to the shear yield stress of the material τ_c along the sticking region, whereas the shear stress in the sliding region is equal to the product of the local friction coefficient and the normal stress, according to the Coulomb friction law. This can be expressed by:

$$\tau_{friction} = \begin{cases} \tau_c & 0 \le x \le l_p \\ \mu_{local} \cdot P & l_p \le x \le l_c \end{cases} \tag{2.23}$$

In this thermo-mechanical dual-zone model there are two different friction coefficients that are defined on the rake contact, the apparent or global friction coefficient μ, due to the total cutting forces acting on the rake face (see equation (2.13)), and the local friction coefficient μ_{local} that is only due to the forces acting on the sliding region on the rake face. This local friction coefficient has also been subject to study. While Merchant considered the apparent friction coefficient equal to the local friction coefficient, Childs et al. showed that the local friction coefficient describing the sliding part of contact can be greater that the apparent friction coefficient and can exceed unity. Another experimental tendency underlines the fact that the local friction coefficient increases with the increase of the temperature at the tool-chip interface and depends on tool-workpiece properties [11].

Experimental data show that the normal pressure distribution is not uniform but is a decreasing function of x on the tool-chip interface [13]. To account for this fact the distribution of pressure is given by:

$$P(x) = P_0 \left(1 - \frac{x}{l_c}\right)^{\psi} \tag{2.24}$$

Where P_0 is the normal stress exerted on the rake face at the tool tip and ψ is an exponential constant which represents the distribution of the pressure. Bahi et al. [11], by considering a chip equilibrium, reached an expression for the normal stress, P_0:

$$P_0 = 4 \cdot \frac{\psi + 1}{\psi + 2} \cdot \frac{\cos^2 \lambda}{\sin 2\theta} \cdot \tau_S \tag{2.25}$$

As well as an expression for the total length of contact, l_C:

$$l_c = \frac{\psi + 2}{2} \frac{\sin(\theta)}{\sin \phi \cdot \cos \lambda} \cdot t_1 \tag{2.26}$$

Ozlu, Budak and Molinari observed that the length of the sliding contact strongly depends of the cutting speed and for high cutting speeds the contact is mainly sliding whereas the sticking zone can be up to 30% of the total contact at low speeds [10]. In order to estimate the length of the sticking zone at the tool-chip interface, several empirical laws have been used in the literature. In Karpat and Ozel [14], this length is considered to be proportional to the chip thickness, Kato suggested that the sticking part is equal to the chip thickness [9], Andreev and Stephenson proposed that the tool-chip contact is divided by two equal parts, and Abuladze proposed an empirical relation to estimate the length of the sticking zone, l_p [11].

2.1.5. **Wear model**

The understanding of the temperature distribution along the tool-workpiece interface at the presence of tool wear helps to provide insight into several important issues in metal cutting, such as tool wear progression, dimensional tolerance and workpiece surface integrity [15].

Karpat and Ozel [16], assumed that the worn flank face is parallel to the cutting direction, the actual (measured) cutting forces in the cutting and thrust directions, F_C and F_T (see figure 2.4), during the machining are the superposition of the wear forces and the cutting forces from shearing. Therefore they expressed these forces, for the case of zero clearance angle, as:

$$F_C = F_{C_S} + F_{C_W} \tag{2.27}$$

$$F_T = F_{T_S} + F_{T_W} \tag{2.28}$$

This superposition of forces is widely accepted due to the observation of many researchers that flank wear does not affect the shear angle. However, reports have been made of plastic flow below worn tool flank when a negative clearance angle exists which creates some doubt about the validity of this approach outside of the zero clearance angle case. Following the Waldorf's approach, they calculated these wear forces by integrating the stress distributions under the flank wear area, considering the stress distribution to have a polynomial shape until it reached a critical point at which the plastic flow began (figure 2.8).

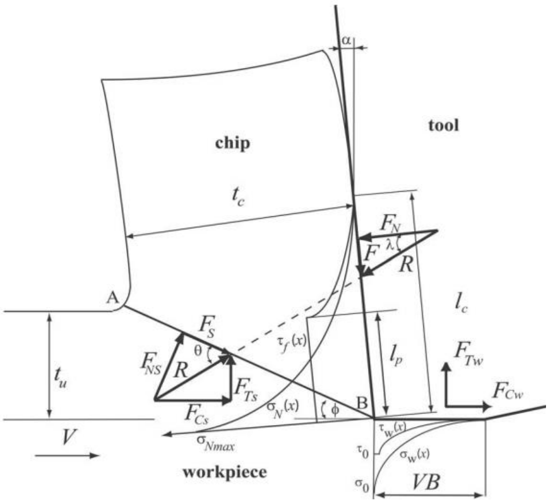

Figure 2.8 – Forces acting on the shear plane, the rake, and on the worn faces of the tool [16].

The stress distributions under the flank wear area by Waldorf can be given by [17]:

$$\tau_{wear} = \begin{cases} \tau_0 & 0 \leq x \leq \mathrm{VB} \cdot \left(1 - \sqrt{\dfrac{\tau_0}{\sigma_0}}\right) \\ \mu \cdot \sigma_w & \mathrm{VB} \cdot \left(1 - \sqrt{\dfrac{\tau_0}{\sigma_0}}\right) \leq x \leq \mathrm{VB} \end{cases} \tag{2.29}$$

Where μ is the known friction coefficient and the values of σ_w, τ_0 and σ_0, can be given by:

$$\sigma_w = \sigma_0 \cdot \left(\frac{VB - x}{VB}\right)^2 \tag{2.30}$$

$$\tau_0 = k \cdot \cos(2\gamma - 2\Phi) \tag{2.31}$$

$$\sigma_0 = k\left[1 + \frac{\pi}{2} - 2\rho - 2\Phi + 2\gamma + \sin(2\gamma - 2\Phi)\right] \tag{2.32}$$

Where k is the shear flow stress and γ can be given by:

$$\gamma = n_p + \Phi - \sin^{-1}\left[\sqrt{2} \cdot \sin\rho \cdot \sin n_p\right] \tag{2.33}$$

2.1.6. **Thermal model**

The modeling of machining temperatures has attracted many researchers because of the complexity of measuring temperatures during machining. Some of these researchers assumed the material on either side of the shear plane as two separate bodies in sliding contact, while others assumed the material to be a single body in front and behind the heat source. The main differences in these models include the assumptions made, the boundary conditions, the direction of motion of the heat source, and the estimation of the heat partition ratio.

Pioneering studies were performed by several researchers most prominent among them are:

Trigger and Chao [18], by developing a steady state two-dimensional analytical model for the prediction of average temperature in metal cutting, they calculated the average temperature rise of the chip as it leaves the shear plane and the average tool-chip interface temperature in orthogonal machining, based on the existence of two heat sources, one on the shear plane and the other on the tool-chip interface, with shear and frictional energy distributed uniformly. They assumed that the latent heat stored in the chip was approximately 12,5% of the total heat generation, and that 90% of the heat would flow into the chip while the rest would go into the work material. They also assumed no redistribution of the thermal shear energy going to the chip during the very short time the chip was in contact with the tool, while at the shear plane the distribution of the thermal energy was computed by using Blok's partition principle. Additionally, they considered the frictional heat source at the tool-chip interface to be a moving band heat source in relation to the chip and a stationary plane source in relation to the tool, with the work surface and the machined surface as adiabatic boundaries (figure 2.9).

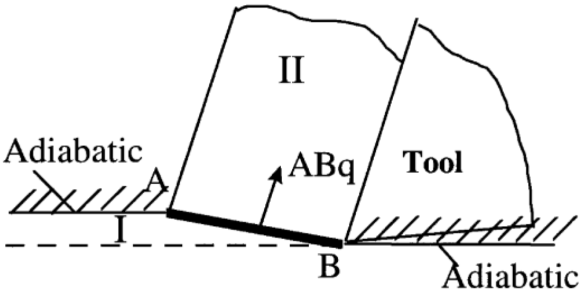

Figure 2.9 – Trigger and Chao’s model [19].

Loewen and Shaw [18], made the same assumptions as Trigger and Chao in order to calculate the average temperature rise at the tool-chip interface and also applied Blok’s heat partition principle. But they considered two bodies, chip and work material, in relative motion at the shear plane. The chip was stationary, considering the shear plane, while the work material was a moving body moving at the velocity of shear instead of the cutting velocity. They obtained two solutions for the temperature rise for each heat source, one for each side of the plane heat source, but since they also considered the tool-chip interface as adiabatic, the shear plane contributes only to the temperature rise in the chip, including the tool-chip interface on the chip side but not on the tool (figure 2.10).

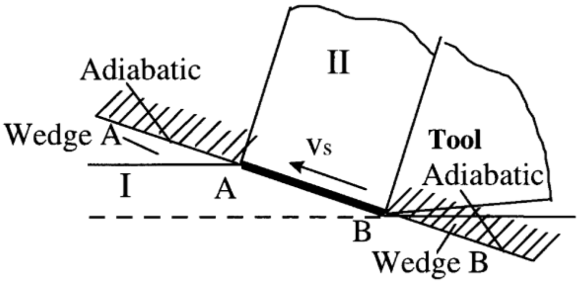

Figure 2.10 – Loewen and Shaw’s model [19].

Leone [19], in a model similar to Loewen and Shaw’s, assumed the shear plane heat source to be parallel to the cutting velocity, ie, shear angle zero since it is usually small, moving in the direction of cutting at the cutting velocity, converting the chip formation process in a frictional sliding contact problem (figure 2.11).

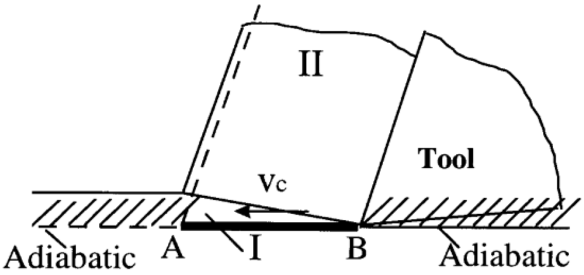

Figure 2.11 – Leone's model [19].

Weiner [18], considered the shear plane as an inclined plane with the heat source moving with a speed equal to the cutting speed, simplified the geometry of the problem by assuming that the chip flow was normal to the shear plane, that the heat conduction in the direction of tool motion was negligible, and finally that the intersection between the shear plane and workpiece free surface remained at ambient temperature (figure 2.12).

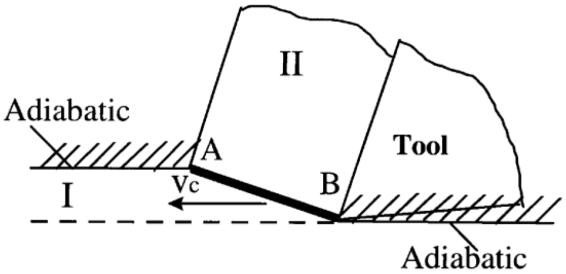

Figure 2.12 – Weiner's model [19].

Chao and Trigger [18], analyzing the previous models found that with the assumption of a uniform heat flux at the tool-chip interface it was impossible to match the temperatures on the two sides of the heat source, the heat flux distribution having necessarily to be non-uniform. They then proposed an approximate analytical procedure in which the heat flux was assumed as an exponential function, obtaining a more realistic interface temperature distribution but found the process time consuming due to it being a cut-and-try procedure. They also tried a discrete numerical iterative method, which involved a combination of analytical and numerical methods as well as Jaeger's solution for the moving and stationary heat sources.

On one hand, the use of Blok's evaluation, of the average temperature at the interface between two bodies in sliding contact (one stationary and the other moving at relative velocity), when applied to the shear plane, despite enabling the use of Jaeger's solution, was also a point of doubt because there is only one body involved, namely, the work material deforming plastically at the shear zone to form the chip. On the other hand, the use of average temperature at the shear zone for the heat partition is not accurate as the temperature varies throughout the length of the shear plane from the tool tip to the chip work-material intersection. And so, the determination of temperature distribution instead of the average temperature should be more useful. This had already been tried by Hahn, although unsuccessfully, the main reason being the lack of computational power as it was computationally intensive [19].

Hahn [19], used an oblique moving band heat source model based on the nature of the chip formation process by, instead of using a simplified model to avoid compensation for the flow of heat carried by the material, considering that the depth of the layer removed from the work material passes continuously through the shear plane thereby undergoing extensive plastic deformation to form the chip (figure 2.13a). This led to the consideration that the shear plane is a band heat source moving in the work material obliquely at the velocity of cutting (figure 2.13b). Also, the material in front and behind the heat source are considered as one continuous body, thus, the heat transfer by conduction and that due to material flow are considered simultaneously.

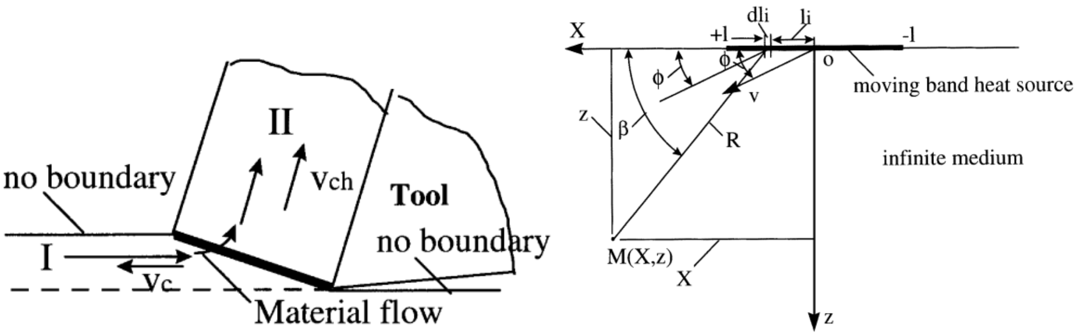

Figure 2.13 – a) Hahn’s model [19]. b) Schematic of Hahn’s model [19].

In this model the moving band heat source is considered as a combination of infinitely small differential segments dl_i, each of which is considered as an infinitely long moving line heat source. Thus, the solution for an infinitely long moving line heat source in an infinite medium can be used for calculating the temperature rise at any point M caused by a differential segment dl_i. Hence the temperature rise at any point M is given by [19]:

$$T_M = \frac{q}{2 \cdot \pi \cdot \lambda_c} e^{-X \cdot V/(2 \cdot a_c)} \cdot K_0 \left(\frac{R \cdot V}{2 \cdot a_c}\right) \tag{2.34}$$

Where q is the heat liberation intensity of the heat source, a_c is the thermal diffusivity and λ_C is the thermal conductivity of the chip material, and K_0 is a Bessel function of the second kind and zero order.

And so, the temperature rise at point M caused by the entire moving band heat source is given by:

$$T_M = \frac{q}{2 \cdot \pi \cdot \lambda_c} \int_{-l}^{+l} e^{-X \cdot V/(2 \cdot a_c)} \cdot K_0 \left(\frac{R \cdot V}{2 \cdot a_c}\right) dl_i \tag{2.35}$$

Komanduri and Hou [19], developed an analytical model for the temperature distribution near the shear zone based on Hahn’s approach focusing, both in the chip and in the work material, incorporating appropriate image sources. They considered the shear plane as an infinitely long oblique plane heat source moving with the cutting velocity, extended the work material past the shear zone as an imaginary area to determine the temperature rise distribution in the work material (figure 2.14a), and extended the chip into the work material past the shear plane as an imaginary area to determine the temperature rise distribution in the chip (figure 2.14b).

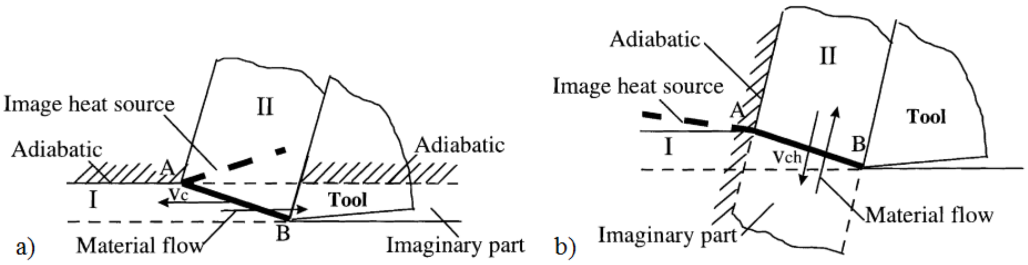

Figure 2.14 – Komanduri and Hou’s model for thermal analysis of a) Work material b) Chip [19].

Komanduri and Hou also modified Hahn’s model to take into consideration the effect of the boundaries and the use of appropriate image sources, incorporating a mirror image of the primary heat source with respect to the adiabatic surface boundary as seen in figure 2.14.

These researchers also determined the temperature rise in the moving chip as well as in the stationary tool due to frictional heat source at the chip-tool interface by using functional analysis. They developed an analytical model that incorporates two modifications to the classical solution of Jaeger’s moving band (for the chip, figure 2.15a) and stationary rectangular (for the tool, figure 2.15b) heat sources for application to orthogonal metal cutting [20].

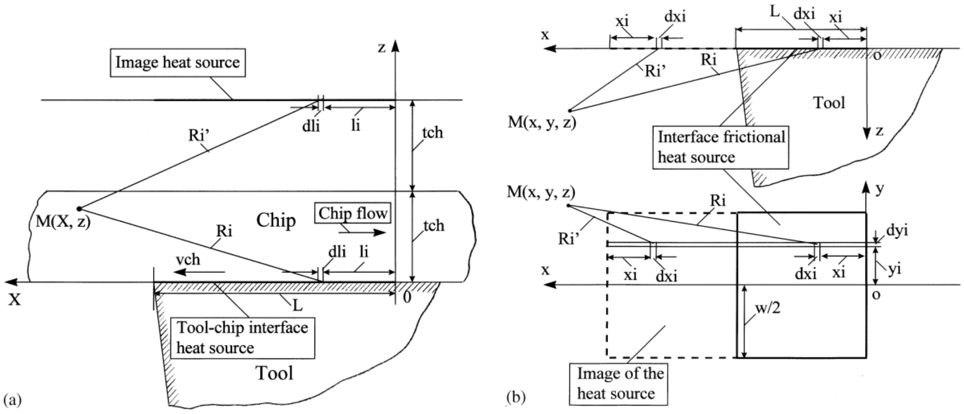

Figure 2.15 – Schematic of the model [20] a) On the chip side (moving band) b) On the tool side (stationary rectangular)

In the chip, the total temperature rise at any point M(X,z) caused by the entire moving interface friction heat source, including its image source, is given by:

$$T_M = \frac{q}{\pi \cdot \lambda_c} \int_{-l}^{+l} e^{-(X-l_i)\cdot V/(2\cdot a_c)} \cdot \left[K_0\left(\frac{R_i \cdot V}{2 \cdot a_c}\right) + K_0\left(\frac{R_i' \cdot V}{2 \cdot a_c}\right)\right] dl_i \tag{2.36}$$

It should be noted that since the interface boundary between the tool and the chip was considered as adiabatic, the solution used should be for a semi-infinite medium, and since the heat source is entirely on the boundary surface, the solution for a semi-infinite medium was considered to be twice that for an infinite medium [20]. On the other hand, the small values of the chip thickness when considered with an adiabatic boundary on the upper surface of the chip justified an image heat source of the friction heat source.

While in the tool, the total temperature rise at any point M(X,z) caused by the entire stationary rectangular interface friction heat source, including its image source, is given by:

$$T_M = \frac{q}{2 \cdot \pi \cdot \lambda_t} \int_{-w/2}^{w/2} \int_0^L \left(\frac{1}{R_i} + \frac{1}{R_i'} \right) dx_i \, dy_i \tag{2.37}$$

They also took into account a non-uniform distribution of the heat partition fraction along the tool-chip interface in order to match the temperature distribution both on the chip side and the tool side by, instead of using only linear functions in the heat partition of variable intensity (figure 2.16a), using a pair of power functions (figure 2.16b):

$$B_{i,chip} = \left(B_{chip} - \Delta B\right) + 2 \cdot \Delta B \cdot \left(\frac{l_i}{L}\right)^m + C \cdot \Delta B \cdot \left(\frac{l_i}{L}\right)^k \tag{2.38}$$

$$B_{i,tool} = \left(B_{tool} + \Delta B\right) - 2 \cdot \Delta B \cdot \left(\frac{l_i}{L}\right)^m - C \cdot \Delta B \cdot \left(\frac{l_i}{L}\right)^k \tag{2.39}$$

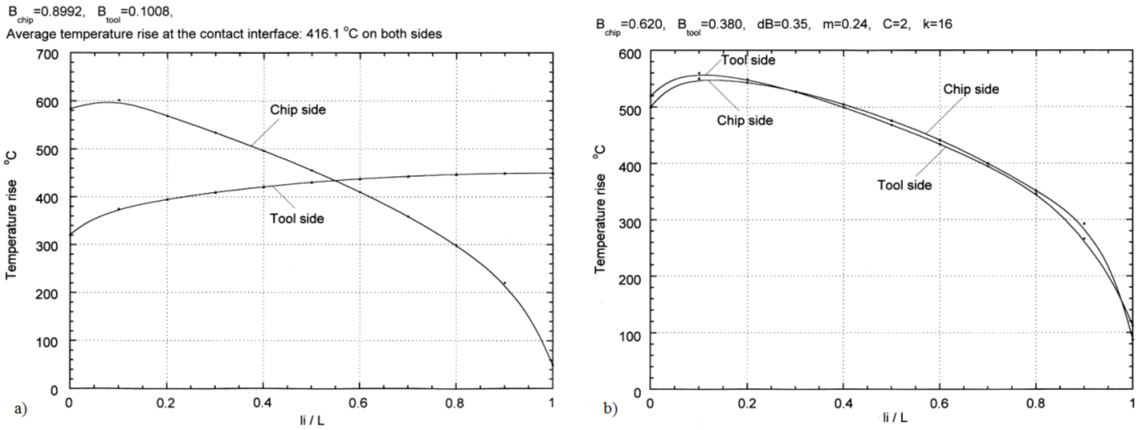

Figure 2.16 – Heat partition fraction a) Using linear functions b) Using a pair of power functions. [20] in the heat partition.

Thus obtaining a reasonably good match of the two temperature distribution curves for the chip side and the tool side [20].

3

PROPOSED MODELS

This chapter presents an analytical and numerical model for each case of temperature rise involved in orthogonal cutting. These models should be sensible to the coupling effects of the variation of mechanical parameters, as well as to the variation of thermo-physical and cutting parameters, in order to obtain results affected by as many relevant parameters, and with as little assumptions and suppositions as possible.

3.1. Analytical and numerical model

As seen in chapter 2, Weber *et al*. considered a comprehensive constitutive model for the work material. This model was used in the proposed model to describe the behavior of the material, but since it takes into account the coupling effects of strain and strain-rate, strain and temperature or strain rate and temperature, it is necessary to determine the state of the material being cut before calculating the temperature rise of the process. With this objective in mind a cycle was developed to calculate the average temperature of the chip in the shear plane, this value is then compared to the value used to start the cycle (which is needed to input the mechanical properties). The cycle will compute until an admissible variation is found. The analytical models to calculate the temperature rise in this work were based on the works by Komanduri and Hou [19-21].

The placement of each pair of axis in each different model is crucial to the good response of the numerical model due to the functions involved. Multiple solutions were tested but only the ones chosen will be shown in this work.

3.1.1. **Temperature rise in the chip**

The temperature rise in the chip is attributed to shear and friction heat sources. The surface of the chip opposed to the tool is considered an adiabatic boundary and because of this, an image heat source with the same intensity as the shear heat source as well as another with the same intensity as the friction heat source are added at mirrored distance (figure 3.1).

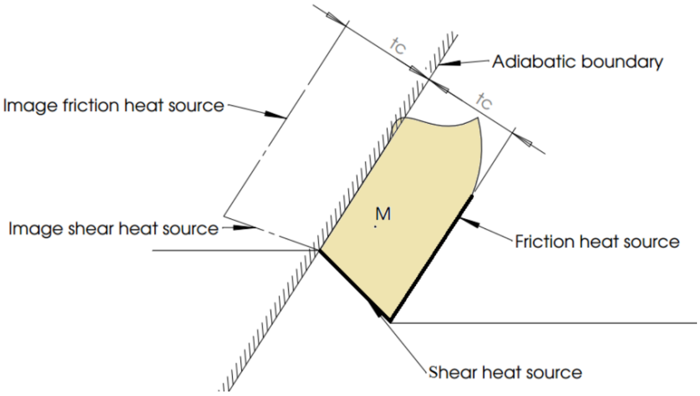

Figure 3.1 – Contributions to the temperature rise in the chip.

This model then leads to the following schematic for the contribution of the shear heat source and its image heat source:

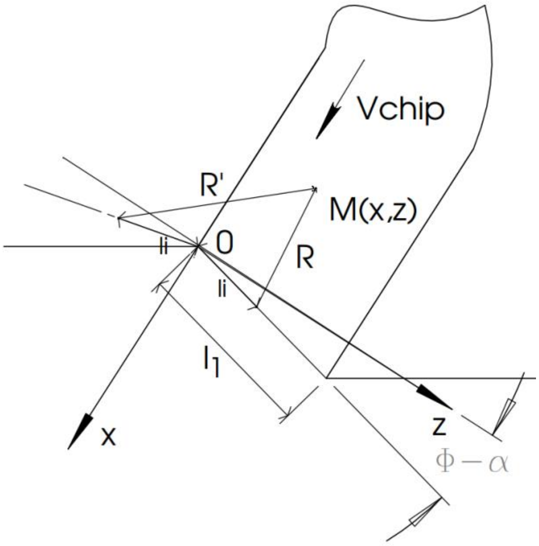

Figure 3.2 – Schematic for the numerical model of the shear heat source and its image source in the chip.

By modifying the equation (2.35) for this case, the temperature rise in the chip due to the shear heat source and its image source is given by:

$$T_{shear\ chip}\ (x,z) = \frac{q_{shear}}{2\cdot\pi\cdot\lambda_c}\int_0^{l_1} e^{-(x-l_i\cdot\sin(\Phi-\alpha))\cdot V/(2\cdot a_c)}\cdot K_0(R)+K_0(R')\ dl_i \tag{3.1}$$

Where the distance R and R’ are given by:

$$R = \frac{V}{2\cdot a_c}\cdot\sqrt{(x-l_i\cdot\sin(\Phi-\alpha))^2+(z-l_i\cdot\cos(\Phi-\alpha))^2} \tag{3.2}$$

$$R' = \frac{V}{2\cdot a_c}\cdot\sqrt{(x-l_i\cdot\sin(\Phi-\alpha))^2+(z+l_i\cdot\cos(\Phi-\alpha))^2} \tag{3.3}$$

In this model the velocity considered is the chip velocity, ie, $V=V_{chip}$.

K_0 is the modified zero order Bessel function of second kind shown in figure 3.3.

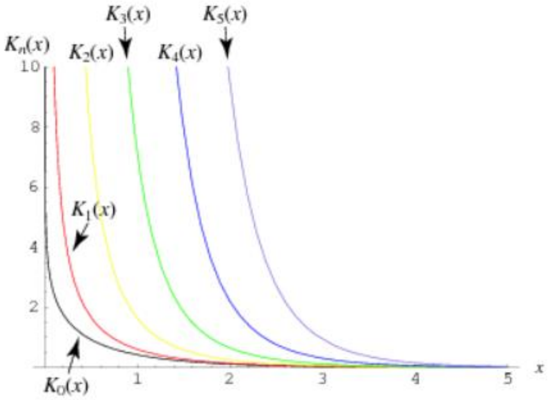

Figure 3.3 –Modified Bessel function of the second kind. [22, 23]

The heat liberation intensity of the heat source in the shear zone is determined by the product of the shear stress along the shear plane (equation (2.20)) and the velocity across the shear plane (equation (2.9)):

$$q_{shear} = \tau_S \cdot V_S \tag{3.4}$$

The model from figure 3.1 also leads to a schematic for the contribution of friction heat source as well as its image heat source:

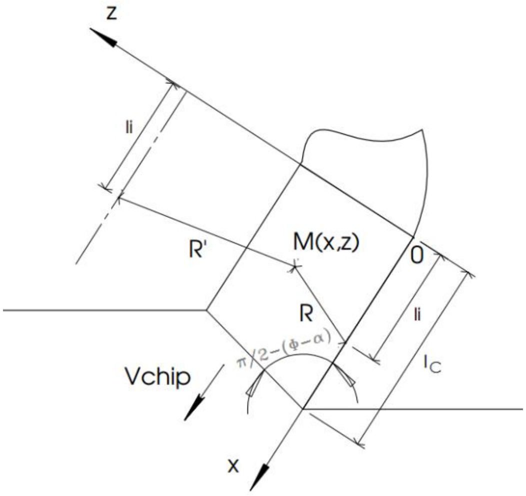

Figure 3.4 – Schematic for the numerical model of the friction heat source and its image source in the chip.

By modifying the equation (2.36) for this case and using the heat partition fraction function, the temperature rise in the chip due to the friction heat source and its image source is given by:

$$T_{friction\ chip}\ (x,z) = \frac{1}{\pi \cdot \lambda_c} \int_0^{l_c} q_{friction} \cdot B_{chip} \cdot e^{-(x-l_i)\cdot V/(2\cdot a_c)} \cdot [K_0(R) + K_0(R')]\ dl_i \tag{3.5}$$

Where the distance R and R’ are given by:

$$R = \frac{V}{2 \cdot a_c} \cdot \sqrt{(x - l_i)^2 + z^2} \tag{3.6}$$

$$R' = \frac{V}{2 \cdot a_c} \cdot \sqrt{(x - l_i\,)^2 + (2 \cdot t_c - z)^2} \tag{3.7}$$

In this model the velocity considered is the chip velocity, ie, V=V$_{chip}$. Since Zorev's model was used to demonstrate the sliding/sticking behavior of the material on the rake face, the chip outflow in the stagnant region will forcefully have to be affected, and so, the assumption is made that even though the chip material along the rake face is represented by a continuous outflow, in the sticking zone the chip flow velocity has a non-uniform distribution defined by a power function of the second degree, the chip velocity is then defined as follows:

$$V_{chip}(li) = \begin{cases} V_{chip} \cdot \left(\frac{x}{l_p}\right)^2 & 0 \leq\ x \leq l_p \\ V_{chip} & l_p \leq x \leq l_c \end{cases} \tag{3.8}$$

The heat liberation intensity of the friction heat source is determined by the product of the friction stress along the rake face and the chip velocity across the rake face:

$$q_{friction}(li) = \tau_{friction}(li) \cdot V_{chip}(li) \tag{3.9}$$

Where $\tau_{friction}$ is given (from equation (2.23)) by the expression:

$$\tau_{friction} = \begin{cases} \tau_c & 0 \leq\ x \leq l_p \\ \mu_{local} \cdot P & l_p \leq x \leq l_c \end{cases} \tag{3.10}$$

While some of the variables are known using equations (2.24), (2.25), and (2.26), others needed to be estimated, namely the local friction coefficient and the length of the sticking zone.

The local friction coefficient can be given by:

$$\mu_{local} = \frac{\tan\lambda \cdot {l_c}^{\psi+1}}{(l_c + l_p \cdot \psi) \cdot (l_c - l_p)^{\psi}} \tag{3.11}$$

The details for this formulation can be found in the Appendix A, nevertheless, l$_c$ is the total contact length, l$_p$ is the sticking zone length, and ψ is an exponential constant which represents the distribution of the pressure and is selected as 2 in the current study.

In this work, in order to avoid an empirical estimate or new assumption, an expression was derived from other equations obtaining a new formulation for the length of the sticking zone, this derivation can also be found in the Appendix A, and is given by:

$$l_p = \left(4 \cdot \frac{\psi + 1}{\psi + 2} \cdot \frac{\cos^2\lambda}{\sin 2\theta} \cdot \tan\lambda \cdot \frac{\tau_S}{\tau_C} \cdot l_c - l_c\right) \frac{1}{\psi} \tag{3.12}$$

In the derivation to this expression it was necessary to know the equations for the normal force acting on the rake face F_{Normal} and for the frictional force on the rake face F_{Frict} (see figure 2.4), from [10], they are given as follows:

$$F_{Normal} = \int_0^{l_C} P(x)\,dx = \int_0^{l_C} P_0 \left(1 - \frac{x}{l_c}\right)^{\psi} \cdot W\,dx = P_0 \frac{W \cdot l_C}{\psi + 1} \tag{3.13}$$

$$\begin{aligned} F_{Frict} &= \int_0^{l_P} \tau_S \cdot W\,dx + \int_{l_P}^{l_C} \tau_S \cdot \left(1 - \frac{x - l_P}{l_c}\right)^{\psi} \cdot W\,dx \\ &= \mu_{local} \cdot P_0 \cdot W \cdot \left(1 - \frac{l_P}{l_c}\right)^{\psi} \cdot \left(l_P + \frac{l_C - l_P}{\psi + 1}\right) \end{aligned} \tag{3.14}$$

Where W is the width of cut. When studying the forces involved it is also useful to know the value of the shear force, assuming the shear stress distribution at the outflow of the shear plane is uniform, F_S is given by:

$$F_S = \frac{W \cdot t_1}{\sin \Phi} \cdot \tau_S \tag{3.15}$$

In conclusion, figure 3.5 is representative of the behavior of both stress distribution and chip velocity outflow on the chip-tool contact interface due to the friction model that was used in this study.

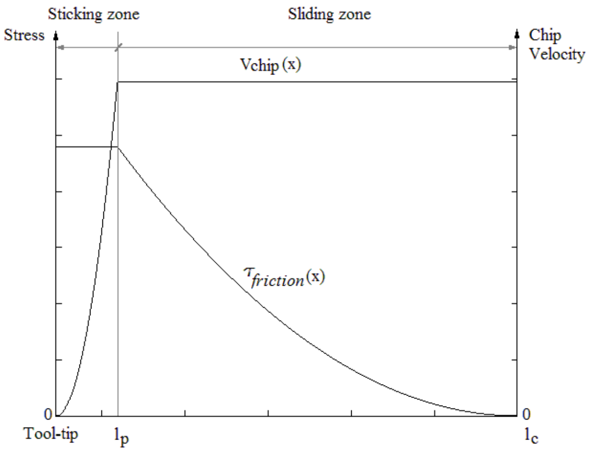

Figure 3.5 - Stress distribution and chip velocity outflow on the chip-tool interface.

Although the heat liberation intensity of the friction heat source varies with this stress distribution and chip velocity at each point in the interface, the temperature rise at that point is also influenced by a heat partition fraction between chip and tool in order to achieve a balance between the temperature at that point by considering a calculation from either the chip or the tool side. As in the work by Komanduri and Hou [19-21], a pair of power functions was used to determine the heat partition fraction between the chip and the tool, one function for each. In this case, the function is:

$$B_{chip}(li) = \left(B_{chip} - \Delta B\right) + 2 \cdot \Delta B \cdot \left(\frac{l_C - l_i}{l_C}\right)^{m} + C \cdot \Delta B \cdot \left(\frac{l_C - l_i}{l_C}\right)^{k} \tag{3.16}$$

It should be noted that the change in the orientation of this function when compared to Komanduri and Hou's is due to the friction heat source being considered an integral of the temperature rise from the end of the contact to the tool-tip, whereas in the Komanduri and Hou's model it was the opposite.

3.1.2. **Temperature rise in the work piece**

The temperature rise in the work piece is attributed to the shear heat source. The surface of the undeformed work piece is considered an adiabatic boundary and due to it, an image heat source with the same intensity as the shear heat source is added (figure 3.6).

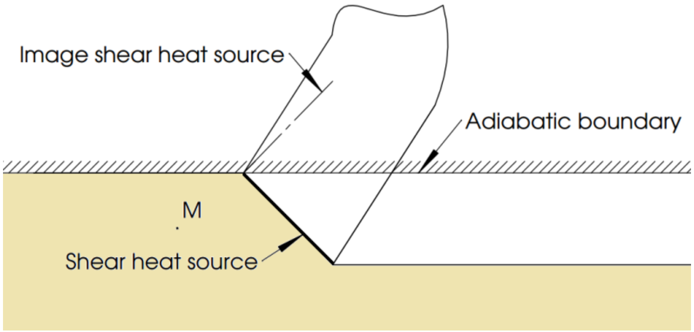

Figure 3.6 – Contributions to the temperature rise in the work piece.

This model then leads to the following schematic for the contribution of the shear heat source and its image heat source:

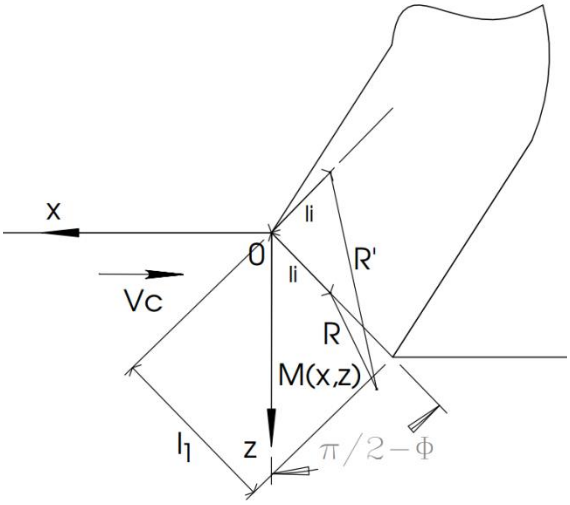

Figure 3.7 – Schematic for the numerical model of the shear heat source and its image source in the work piece.

By modifying the equation (2.35) for this case, the temperature rise in the work piece due to the shear heat source and its image source is given by:

$$T_{shear\ work}\ (x,z) = \frac{q_{shear}}{2\cdot\pi\cdot\lambda_c}\int_0^{l_1} e^{-\left(x+l_i\cdot\sin\left(\frac{\pi}{2}-\Phi\right)\right)\cdot V/(2\cdot a_c)}\cdot[K_0(R)+K_0(R')]\,dl_i \tag{3.17}$$

Where the distance R and R’ are given by:

$$R = \frac{V}{2\cdot a_c}\cdot\sqrt{\left(x+l_i\cdot\sin\left(\frac{\pi}{2}-\Phi\right)\right)^2+\left(z-l_i\cdot\cos\left(\frac{\pi}{2}-\Phi\right)\right)^2} \tag{3.18}$$

$$R' = \frac{V}{2\cdot a_c}\cdot\sqrt{\left(x+l_i\cdot\sin\left(\frac{\pi}{2}-\Phi\right)\right)^2+\left(z+l_i\cdot\cos\left(\frac{\pi}{2}-\Phi\right)\right)^2} \tag{3.19}$$

In this model the velocity considered is the cutting speed, ie, $V=V_C$.

3.1.3. Temperature rise in the tool

The temperature rise in the tool is attributed to the friction heat source in the tool-chip interface, and to induction on the rake face caused by the shear heat source in the form of induction into the tool from the rake face (figure 3.8).

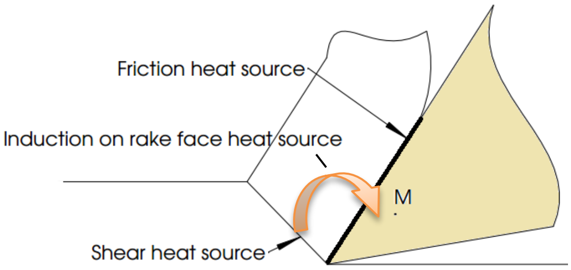

Figure 3.8 – Contributions to the temperature rise in the tool.

This model then leads to the following schematic for the contribution of the friction heat source:

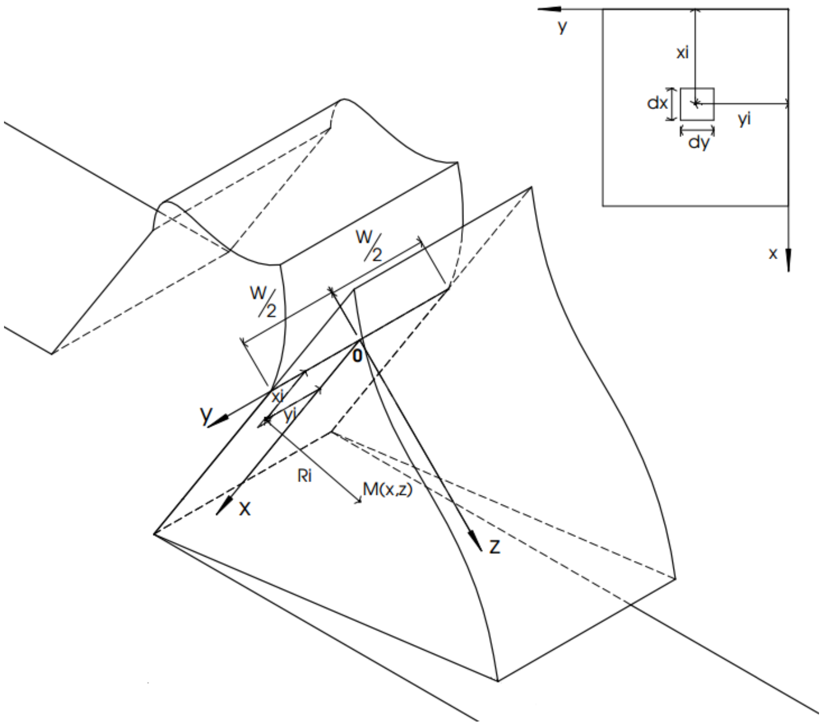

Figure 3.9 – Schematic for the numerical model of the friction heat source in the tool.

Komanduri and Hou considered the clearance face of the tool to be an adiabatic boundary which would imply a mirror image heat source (see figure 2.15), but since a wear model was added to the numerical model it created a contact interface between tool and work piece, and so this mirror image was removed.

By modifying the equation (2.37) for this case, the temperature rise in the tool due to the friction heat source is given by:

$$T_{friction\ tool}\ (x,z) = \frac{1}{\pi \cdot \lambda_t} \int_{-W/2}^{W/2} \int_{0}^{l_C} q_{friction} \cdot B_{tool} \cdot \left(\frac{1}{R_i}\right) dx_i\ dy_i \tag{3.20}$$

It should be noted that once again the interface boundary between the tool and the chip is adiabatic, and since the heat source is entirely on the boundary surface, the solution for a semi-infinite medium was considered to be twice that for an infinite medium. On the other hand, the thermal conductivity λ_t now used is of the tool material.

Where the distance R_i is given by:

$$R_i = \frac{V}{2 \cdot a_c} \cdot \sqrt{(x - x_i)^2 + y_i^2 + z^2} \tag{3.21}$$

The heat liberation intensity of the friction heat source is determined in the same way as to the temperature rise in the chip in chapter 3.1.1.

While the fraction of heat going into the tool from the chip-tool interface is determined by the function:

$$B_{tool}(x_i) = (B_{tool} - \Delta B) + 2 \cdot \Delta B \cdot \left(\frac{l_C - x_i}{l_C}\right)^m + C \cdot \Delta B \cdot \left(\frac{l_C - x_i}{l_C}\right)^k \tag{3.22}$$

It should be noted that the heat partition fraction will vary with x_i but not with y_i, as was considered for the chip.

The model in figure 3.8 also leads to the following schematic for the contribution of the induction on the rake face caused by the shear heat source:

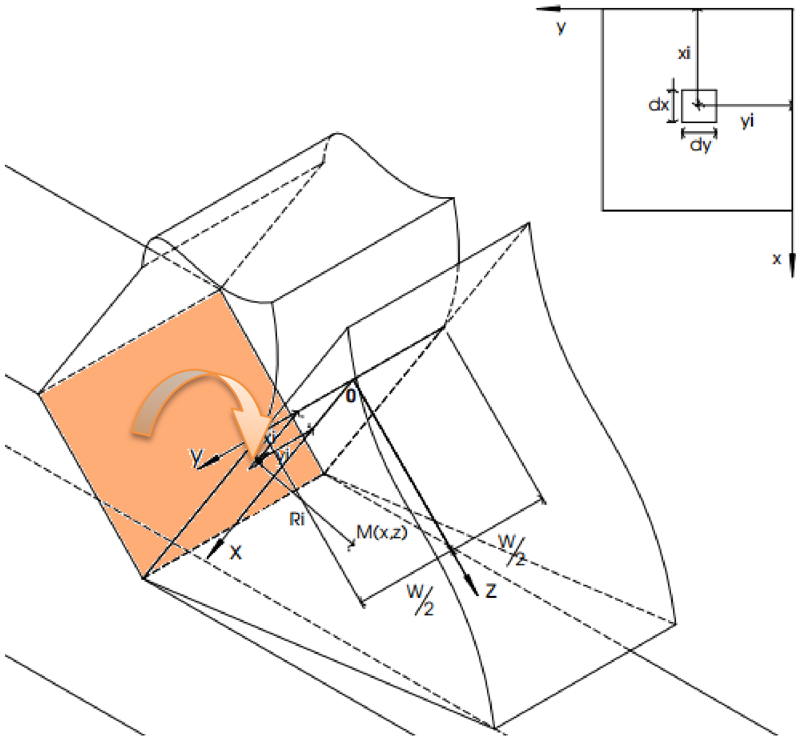

Figure 3.10 – Schematic for the numerical model of the induction on the rake face of the tool caused by the shear heat source.

Where the heat from the shear heat source increases the temperature of the tool due to the heat going by induction from the chip to the tool, this new heat source was considered to be a stationary rectangular zone heat source and therefore an expression similar to equation (3.20) was used, although with a different heat liberation intensity. This expression is given as:

$$T_{induction\ on\ rake\ tool}\ (x,z) = \frac{q_{induction\ on\ rake}}{\pi \cdot \lambda_t} \int_{-W/2}^{W/2} \int_{0}^{l_C} B_{induction\ rake} \cdot \left(\frac{1}{R_i}\right) dx_i\, dy_i \tag{3.23}$$

For the determination of the induction on rake heat liberation intensity it was assumed that the temperature rise would be in equilibrium when considering the chip-tool interface by either side, when only the shear heat source is considered. This is expressed by:

$$\int_0^{l_C} T_{induction\ on\ rake\ tool}\,(x,0)\,dx = \int_0^{l_C} T_{shear\ chip}\,(x,0)\,dx \tag{3.24}$$

The resulting expression due to the combination of equations (3.23) and (3.24) for the induction on rake heat liberation intensity can be given by:

$$q_{induction\ on\ rake} = \frac{\int_0^{l_C} T_{shear\ chip}\,(x,0)\,dx}{\int_0^{l_C} \frac{1}{\pi \cdot \lambda_t} \int_{-W/2}^{W/2} \int_0^{l_C} B \cdot \left(\frac{1}{R_i}\right) dx_i\,dy_i\,dx} \tag{3.25}$$

While the fraction of heat going into the tool by the rake face, due to induction of the shear heat source, is determined by the function:

$$B_{induction\ rake}(x_i) = (B_{ind} - \Delta B_i) + 2 \cdot \Delta B_i \cdot \left(\frac{x_i}{l_C}\right)^{m_i} + C_i \cdot \Delta B_i \cdot \left(\frac{x_i}{l_C}\right)^{k_i} \tag{3.26}$$

3.1.4. Temperature rise due to the wear flank of the tool-tip

When the geometry of the tool is considered to be modified due to wear, some considerations are made, namely the introduction of a flank face which implies a rubbing heat source that affects the temperature rise in the work piece and the tool, and an induction on the flank face heat source caused by the shear heat source that affects the temperature rise in the tool.

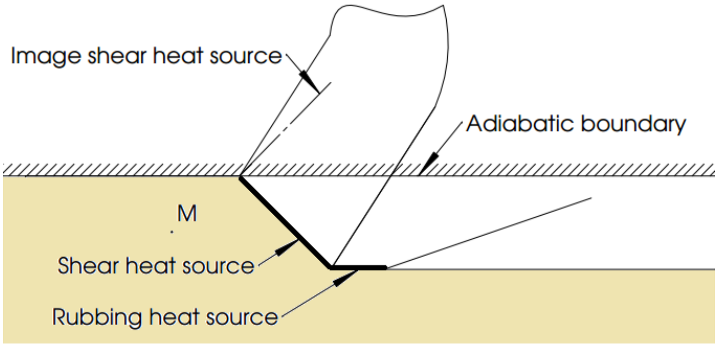

Figure 3.11 – Contributions to the temperature rise in the work piece with a flank face.

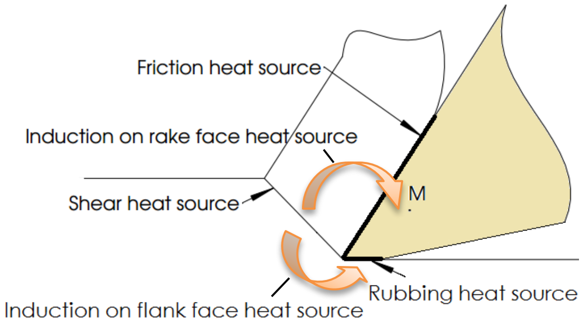

Figure 3.12 – Contributions to the temperature rise in the tool with a flank face.

The contribution of the rubbing heat source in the flank face when considering the work piece leads to the following schematic:

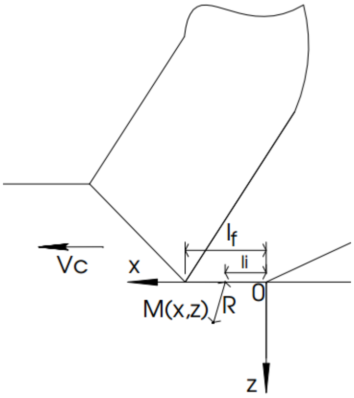

Figure 3.13 – Schematic for the numerical model of the rubbing heat source in the flank face in the work piece.

By considering this to be a similar case to the temperature rise in the chip due to the friction heat source and modifying the equation (3.5) for this case, the temperature rise in the work piece due to the rubbing heat source is given by:

$$T_{rubbing\,work}\,(x,z) = \frac{1}{\pi \cdot \lambda_c} \int_0^{l_f} q_{rubbing} \cdot B_f \cdot e^{-(x-l_i)\cdot V/(2\cdot a_c)} \cdot K_0(R)\,dl_i \tag{3.27}$$

Where the distance R is given by:

$$R = \frac{V}{2 \cdot a_c} \cdot \sqrt{(x - l_i)^2 + z^2} \tag{3.28}$$

In this model the velocity considered is the cutting speed, ie, $V=V_C$.

Since the length of the flank face l_f is dependent on the wear state of the tool it was assumed when testing the numerical model that either the tool was perfectly sharp, with no flank face, or it had the failure value of 0.3 mm according to the criteria recommended by ISO3685:1993 [24].

The heat liberation intensity of the rubbing heat source is determined by the product of the rubbing stress along the flank face and the cutting speed:

$$q_{rubbing}(li) = \tau_{rubbing}(li) \cdot V_c \tag{3.29}$$

Where $\tau_{rubbing}$ is given, from a modification of the equation (2.29) to this case, by the expression:

$$\tau_{rubbing} = \begin{cases} \mu \cdot P_{w^*} \cdot \left(\frac{\mathrm{l}_f - x}{\mathrm{l}_f}\right)^2 & 0 \leq\ x \leq \mathrm{l}_{fc} \\ \mu \cdot P_{w^*} & \mathrm{l}_{fc} \leq x \leq \mathrm{l}_f \end{cases} \tag{3.30}$$

The normal pressure along the flank worn face was determined by adopting the same idea behind equation (3.13) to this case:

$$P_{w^*} = \frac{F_{Ts} \cdot (\psi + 1)}{W \cdot \mathrm{l}_f} \tag{3.31}$$

Where F_{Ts} can be given by the forces diagram shown in figure 2.8:

$$F_{Ts} = R \cdot \sin(\theta - \Phi) \tag{3.32}$$

The resultant force can be given by:

$$R = \frac{F_S}{\cos\theta} \tag{3.33}$$

And F_S previously found by equation (3.15).

The length of the wear flank until critical plastic flow point l_{fc} can be given by:

$$\mathrm{l}_{fc} = \mathrm{l}_f \left(1 - \sqrt{\frac{1}{1 + \frac{\pi}{2}}}\right) \tag{3.34}$$

The formulation of this equation can be found in Appendix B.

A pair of power functions similar to the ones used for the heat partition fraction between the chip and the tool where used for the heat partition fraction between the work piece and the tool, only with different variable values. In this case, it can be given by:

$$B_f(li) = (B_{work} - \Delta B_2) + 2 \cdot \Delta B_2 \cdot \left(\frac{l_i}{\mathrm{l}_f}\right)^{m_2} + C_2 \cdot \Delta B_2 \cdot \left(\frac{l_i}{\mathrm{l}_f}\right)^{k_2} \tag{3.35}$$

The contribution of the rubbing heat source in the flank face when considering the tool leads to the following schematic:

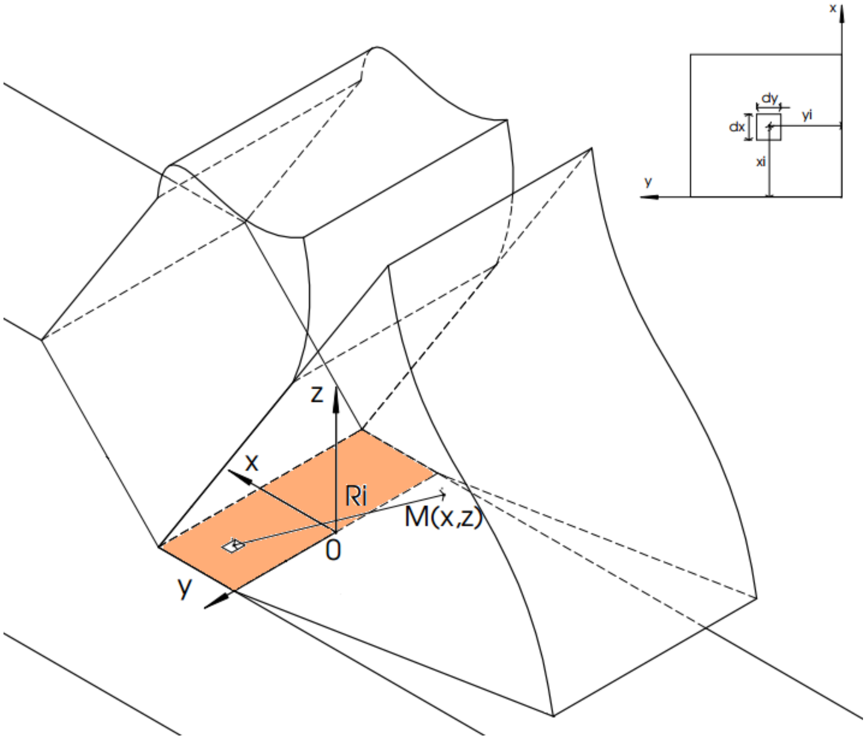

Figure 3.14 – Schematic for the numerical model of the rubbing heat source on the flank face in the tool.

By considering this to be a similar case to the temperature rise in the tool due to the friction heat source and modifying equation (3.20) for this case, the temperature rise in the tool due to the rubbing heat source can be given by:

$$T_{rubbing\ tool}\ (x,z) = \frac{1}{\pi\cdot\lambda_t}\int_{-W/2}^{W/2}\int_{0}^{l_f} q_{rubbing}\cdot(1-B_f)\cdot\left(\frac{1}{R_i}\right)dx_i\,dy_i \tag{3.36}$$

Where the distance R_i can be given by:

$$R_i = \frac{V}{2\cdot a_c}\cdot\sqrt{(x-x_i)^2+y_i^2+z^2} \tag{3.37}$$

The contribution of the induction on the flank face heat source when considering the tool leads to the following schematic:

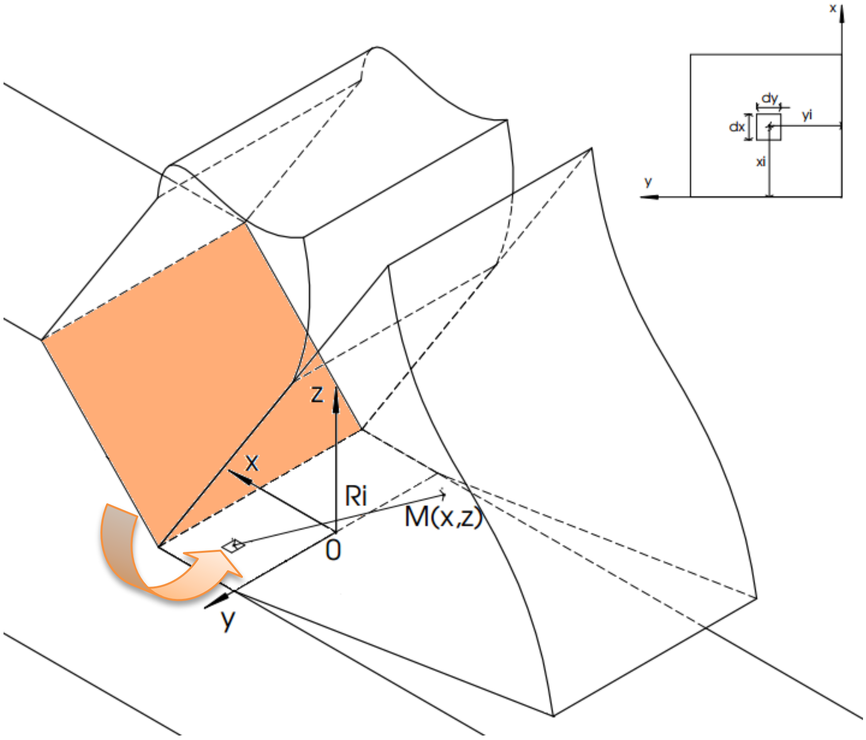

Figure 3.15 – Schematic for the numerical model of the induction on the flank face of the tool caused by the shear heat source.

By considering this to be a similar case to the temperature rise in the tool due to the induction caused by the shear heat source on the rake face and modifying the equation (3.23) for this case, the temperature rise in the tool due to the induction on the flank face heat source can be given by:

$$T_{induction\ on\ flank\ tool}\ (x, z) = \frac{q_{induction\ on\ flank}}{\pi \cdot \lambda_t} \int_{-W/2}^{W/2} \int_{0}^{l_f} (1 - B_f) \cdot \left(\frac{1}{R_i}\right) dx_i\, dy_i \qquad (3.38)$$

Where the distance R$_i$ can be given by:

$$R_i = \frac{V}{2 \cdot a_c} \cdot \sqrt{(x - x_i)^2 + y_i^2 + z^2} \qquad (3.39)$$

For the determination of the induction on flank heat liberation intensity it was assumed that the temperature rise would be in equilibrium when considering the workpiece-tool interface by either side, when only the shear heat source is considered. This is expressed by:

$$\int_{0}^{l_c} T_{induction\ on\ flank\ tool}\ (x, 0)\, dx = \int_{0}^{l_c} T_{shear\ work}\ \left(x, l_1 \cdot \cos\left(\frac{\pi}{2} - \Phi\right)\right) dx \qquad (3.40)$$

The resulting expression due to the combination of equations (3.38) and (3.40) for the induction on rake heat liberation intensity, can be given by:

$$q_{induction\ on\ flank} = \frac{\int_0^{l_C} T_{shear\ work}\ \left(x, l_1 \cdot \cos\left(\frac{\pi}{2} - \Phi\right)\right) dx}{\int_0^{l_C} \frac{1}{\pi \cdot \lambda_t} \int_{-W/2}^{W/2} \int_0^{l_f} (1 - B_f) \cdot \left(\frac{1}{R_i}\right) dx_i\ dy_i\ dx} \tag{3.41}$$

In conclusion , the cycle developed to calculate the average temperature of the chip in the shear plane to determine the state of the material being cut, can be summarized by the following flow chart of what was called the booting program:

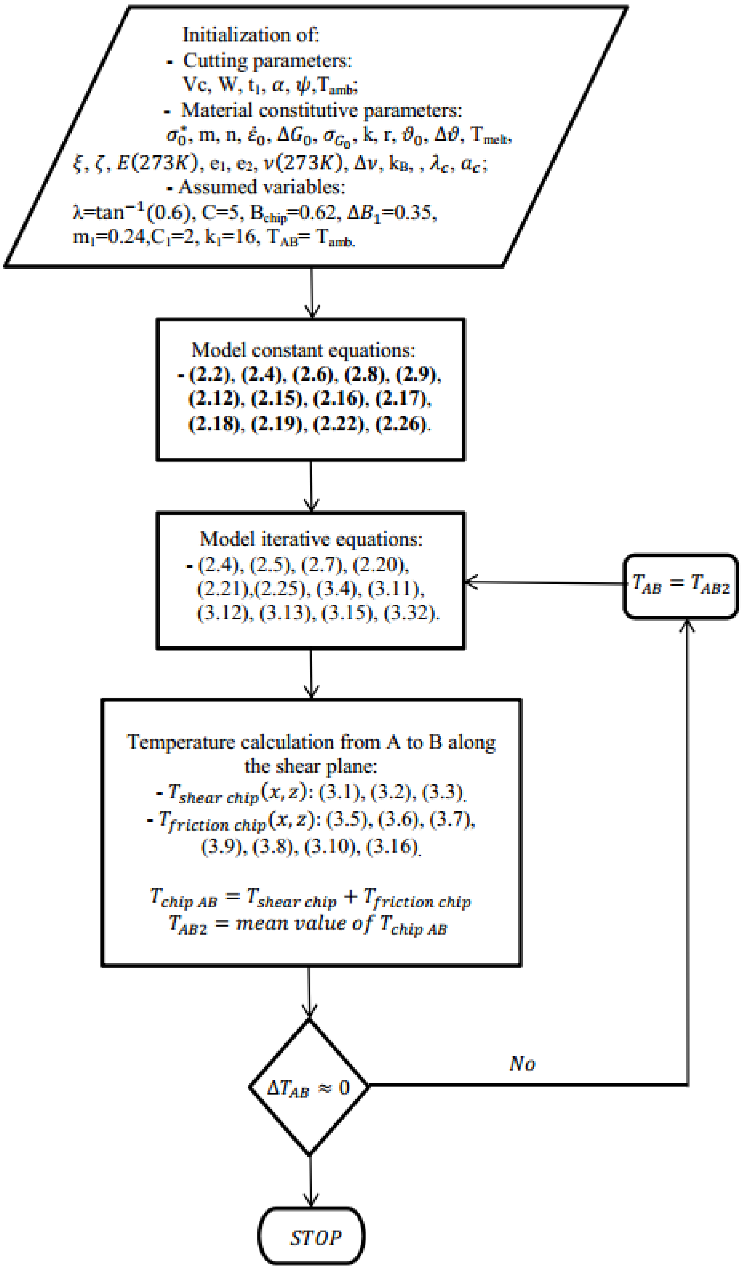

Figure 3.16 – Flow chart of the booting program.

Following the computation of this cycle the temperature rise of the chip, tool and work piece may be found using the models previously explained. The total temperature of the chip can be given by:

$$T_{chip}\ (x,z) = T_{shear\ chip}\ (x,z) + T_{friction\ chip}\ (x,z) + T_{amb} \tag{3.42}$$

The total temperature of the work piece with a perfectly sharp edge can be given by:

$$T_{work\ piece}\ (x,z) = T_{shear\ work}\ (x,z) + T_{amb} \tag{3.43}$$

The total temperature of the tool with a perfectly sharp edge can be given by:

$$T_{tool}\ (x,z) = T_{friction\ tool}\ (x,z) + T_{induction\ on\ rake\ tool}\ (x,z) + T_{amb} \tag{3.44}$$

The total temperature of the work piece with a wear flank can be given by:

$$T_{work\ piece}\ (x,z) = T_{shear\ work}\ (x,z) + T_{rubbing\ work}\ (x,z) + T_{amb} \tag{3.45}$$

The total temperature of the tool with a wear flank can be given by:

$$\begin{aligned} T_{tool}\ (x,z) = {} & T_{friction\ tool}\ (x,z) + T_{induction\ on\ rake\ tool}\ (x,z) + T_{rubbing\ tool}\ (x,z) \\ & + T_{induction\ on\ flank\ tool}\ (x,z) + T_{amb} \end{aligned} \tag{3.46}$$

4

RESULTS AND DISCUSSION

This chapter presents the results found for the calculation of the temperature rise due to the model proposed for each relevant area of study as well as their discussions.

4.1. Initial considerations for the calculation of the temperature rise

Since some of the material parameters involved in the proposed model are very specific and not widely used in studies of this kind, only two materials were considered. These materials are characterized by the table 4.1:

Table 4.1 Material parameters for AISI 1045 and AISI O2 [5]

	AISI 1045	**AISI O2**		**AISI 1045**	**AISI O2**
$\boldsymbol{\sigma_0^*}$ **[MPa]**	2000	1550	$\boldsymbol{\xi}$	2	2
m	1.78	3.23	$\boldsymbol{\zeta}$	9	11
n	0.5	0.57	$\boldsymbol{E(273K)}$ **[MPa]**	$2.1\cdot10^5$	$2.1\cdot10^5$
$\boldsymbol{\dot{\varepsilon}_0}$ **[s^{-1}]**	$4.41\cdot10^7$	$1.75\cdot10^7$	**e$_1$ [MPa K^{-1}]**	-52	-52
$\boldsymbol{\Delta G_0}$ **[Js]**	$1.03\cdot10^{-19}$	$1.82\cdot10^{-19}$	**e$_2$ [MPa K^{-2}]**	$-4.7\cdot10^{-2}$	$-4.7\cdot10^{-2}$
$\boldsymbol{\sigma_{G_0}}$ **[MPa]**	330	920	$\boldsymbol{\nu(273K)}$	0.283	0.283
k [MPa]	435	504	$\boldsymbol{\Delta\nu}$ **[K^{-1}]**	$4\cdot10^{-5}$	$4\cdot10^{-5}$
$\boldsymbol{r}$	0.22	0.14	**k$_B$ [J K^{-1}]**	$1.38\cdot10^{-23}$	$1.38\cdot10^{-23}$
$\boldsymbol{\vartheta_0}$ **[K]**	560	540	$\boldsymbol{\lambda_c}$ **[Wm^{-1} K^{-1}]**	50	46
$\boldsymbol{\Delta\vartheta}$ **[K]**	90	100	$\boldsymbol{a_c}$ **[m^2/s]***	$4.19\cdot10^{-6}$	$8.31\cdot10^{-6}$
T$_{melt}$ [K]	1793	1723	*calculated with data from [25]		

While the AISI 1045 is a medium carbon steel used when greater strength and hardness is desired compared to the “as rolled” condition, the AISI O2 is a cold work tool steel with high dimensional stability at heat treatment and it has a very high resistance to cracking, high machinability, medium toughness and resistance to wear [25].

For the calculation of the temperature in the orthogonal cutting process, the equations referred before were implemented in the software MATLAB for an analysis of the temperature of the chip, tool and work piece.

Since each contribution to the temperature rise is different and involves different equations and a different set of axis, it required a different function for each contribution. Because each function is dependent of the axis considered, it was important to understand the axis position and direction in order to be able to add together the different contributions of the temperature rise referring to the same point in a global coordinate system. For example, for the chip there is a contribution due to shear and a contribution due to friction, each with their respective set of axis, as can be seen in figure 4.1:

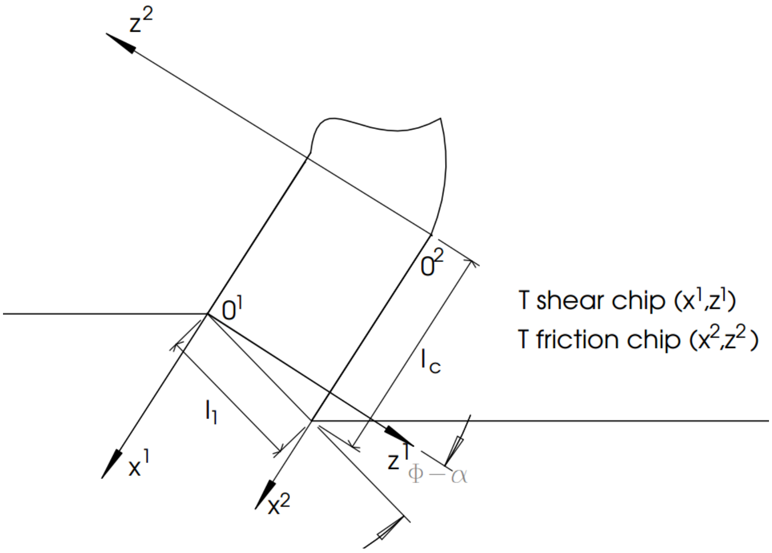

Figure 4.1 – Schematic for the model of the shear and friction heat sources in the chip.

If the point being considered was located at the tool-tip (chip side), the coordinates would be $T_{shear\ chip}\ (l_1 \cdot \sin(\Phi - \alpha)\ ,t_C)$ and $T_{friction\ chip}\ (l_C, 0)$.

On the other hand, since the temperature rise in each point is calculated from the integration of infinitely small differential segments (see chapter 2.1.6), the MATLAB program for each contribution equates that integration to a Riemann sum and a number of intervals was chosen until the temperature rise became independent of it. For example in figure 4.2 the effect the number of divisions of the length of the shear heat source plane has on the temperature of each point in the plane is clear.

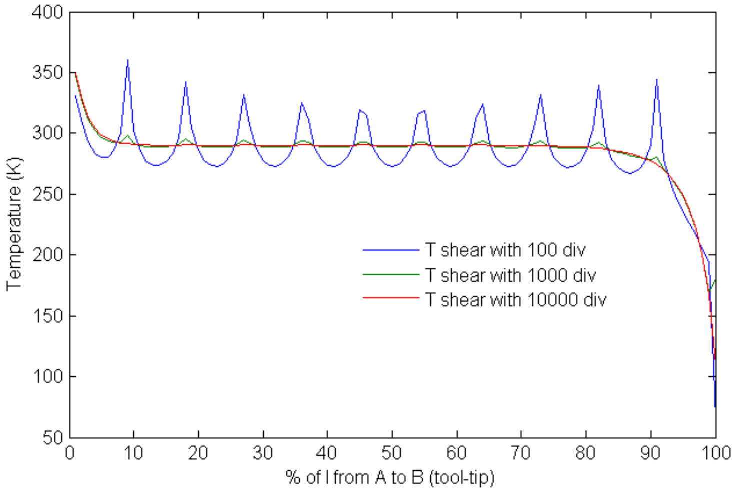

Figure 4.2 – Temperatures of the chip in the shear plane due to shear with different number of divisions.

4.2. Temperature rise along the shear plane

A MATLAB program for the booting cycle (see figure 3.16) was developed in which the material state variables are calculated along the shear plane. These variables are then used as constants on the programs for each temperature rise contribution.

The booting program with input data for the material AISI 1045 took only three iterations to reach a mean value that was close to the temperature used to calculate the constitutive state of the material at the beginning of the cycle. This mean value is the sum of a few contributions (see equation (3.42)) but, taking only into account the temperature rise of the chip in the shear zone, it was found that only the shear heat source is actually relevant as an heat source, the temperature rise due to friction at the rake face being nearly zero as shown in figure 4.3.

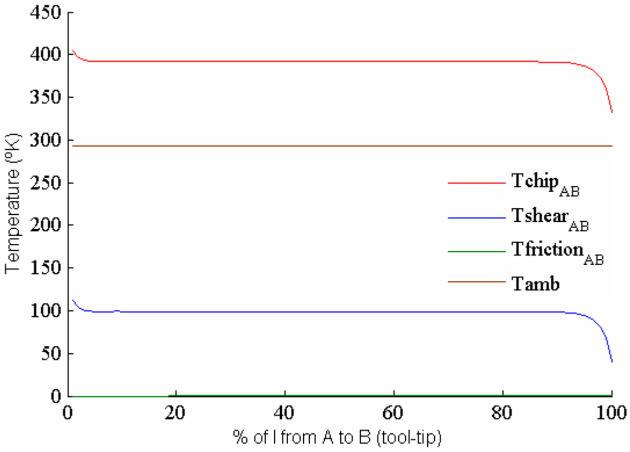

Figure 4.3 – Temperatures of the chip in the shear plane for AISI 1045.

This conclusion is easily explained by the chip only being in contact with the moving band of the friction heat source after going through the shear plane and moving away from it. On the other hand, it should be noted that even though the slight increase of temperature at the end of the shear zone and the decrease near the tool-tip do not influence the mean value since they cancel each other, they can be explained by the adiabatic surface boundary at the end of the shear zone.

For the material AISI O2 the booting program took five iterations and the temperatures mean value of the chip in the shear plane rose significantly, which suggests the program is responsive to the material being studied. The progressions of the temperatures in the chip, follow the same behavior as for the AISI 1045 (figure 4.4).

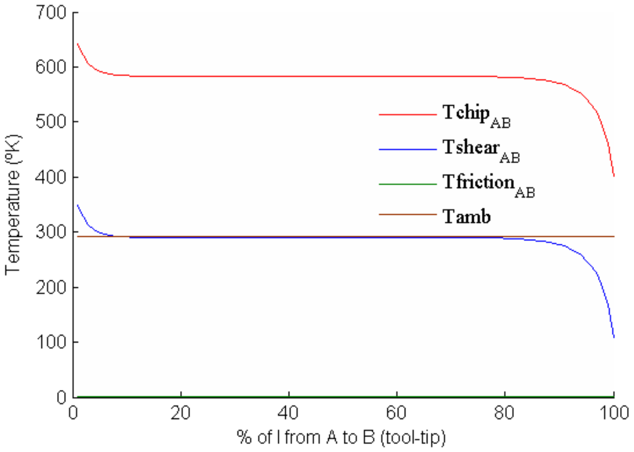

Figure 4.4 – Temperatures of the chip in the shear plane for AISI O2.

Both the temperatures for the AISI 1045 (figure 4.3) and AISI O2 (figure 4.4) were calculated with the cutting parameters in table 4.2:

Table 4.2 Cutting parameters

	AISI 1045	**AISI O2**
Vc [m·s^{-1}]	2	2
W [m]	$2.5\cdot10^{-3}$	$2.5\cdot10^{-3}$
t_1 [m]	$2.5\cdot10^{-4}$	$2.5\cdot10^{-4}$
α [º]	5	5
ψ	2	2
T_{amb} [K]	293	293

4.3. Temperature rise in the chip

Inputting in the model the AISI O2 material parameters and the values for the heat partition equation of the chip (see equation (3.16)) taken from Komanduri and Hou’s work [20], the temperature rise in the chip was calculated. The temperature rise in the interface chip-tool (c-t), on the chip side, due to the shear zone is shown in figure 4.5:

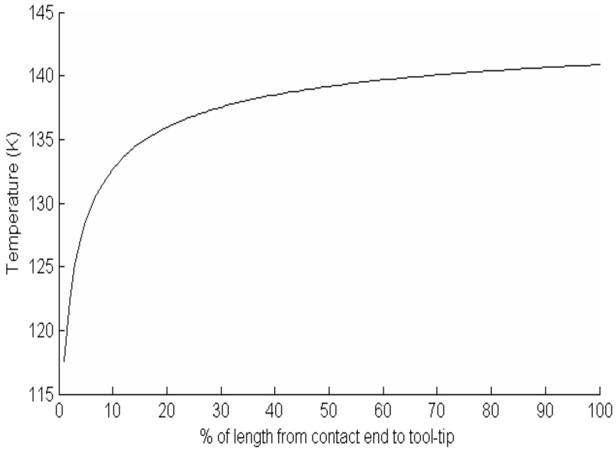

Figure 4.5 – Temperature rise on the interface c-t, chip side, for AISI O2 due to the shear heat source.

As was expected the maximum temperature rise due to the shear heat source is near that heat source, and the furthest from the heat source, the lower the temperature rise is.

When considering the whole chip, the results due to the shear heat source can be seen in figure 4.6:

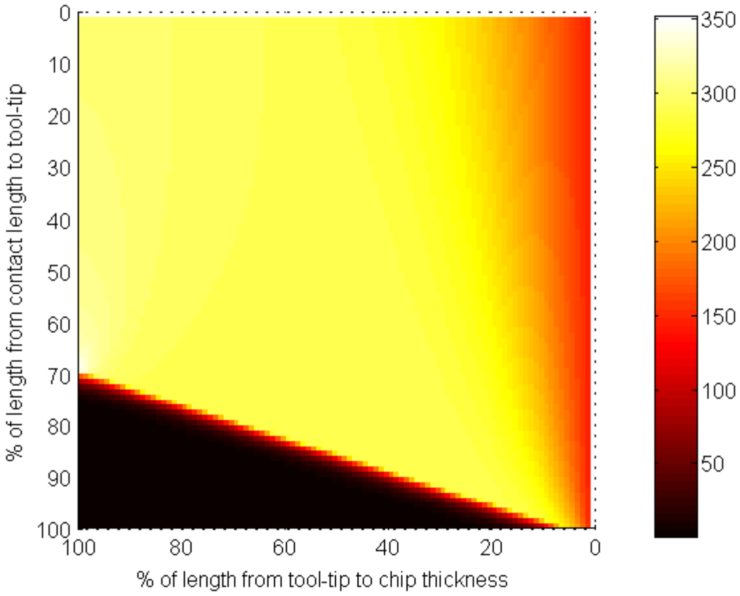

Figure 4.6 – Temperature rise on the chip due to the shear heat source for AISI O2.

As was expected from the results in the temperatures of the chip in the shear plane (figure 4.3) the highest temperature rise is located at the end of the shear plane near to shear heat source and where the adiabatic boundary is located. The temperature rise near the interface of the chip-tool also follows what was expected (figure 4.5), showing a progressively lower temperature rise around the end of the chip-tool contact.

The temperature rise in the interface chip-tool, on the chip side, due to friction is shown in Figure 4.7:

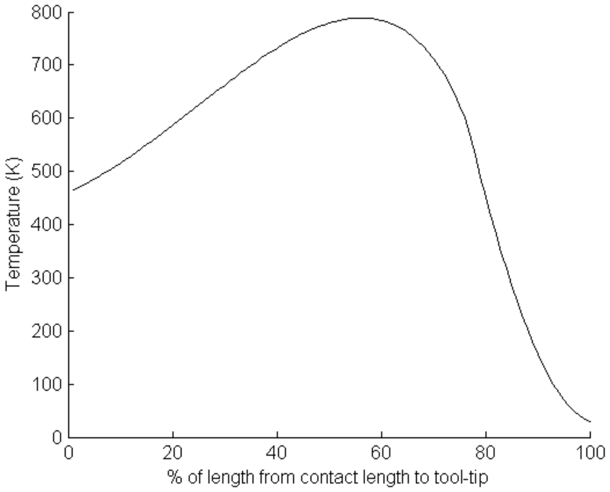

Figure 4.7 – Temperature rise on the interface c-t, chip side, due to the friction heat source for AISI O2.

The temperature rise due to friction is strongly influenced by the friction model (figure 3.5). It starts at the end of c-t contact by increasing until a maximum point near the end of the sticking zone and slowly starts to decrease the value of temperature rise in the sticking zone until a minimum at the tool tip, which was expected since the friction process starts there.

When considering the whole chip, the results due to the friction heat source can be seen in figure 4.8:

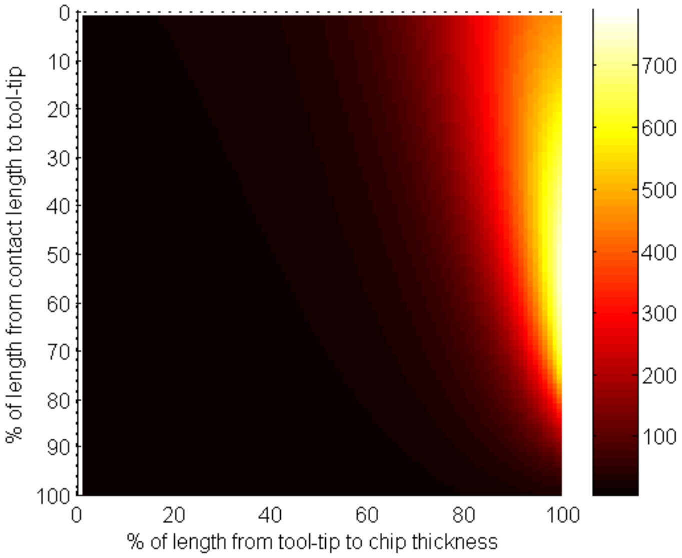

Figure 4.8 – Temperature rise on the chip due to the friction heat source for AISI O2.

Once again, it can clearly be seen the significant importance of the friction model to the model created when friction heat source is being considered. The highest temperature rise can be found near the sticking zones end where the chip velocity and stress distribution are both maximum.

When considering the sum of the contributions (see equation (3.42)), the results are depicted in figure 4.9:

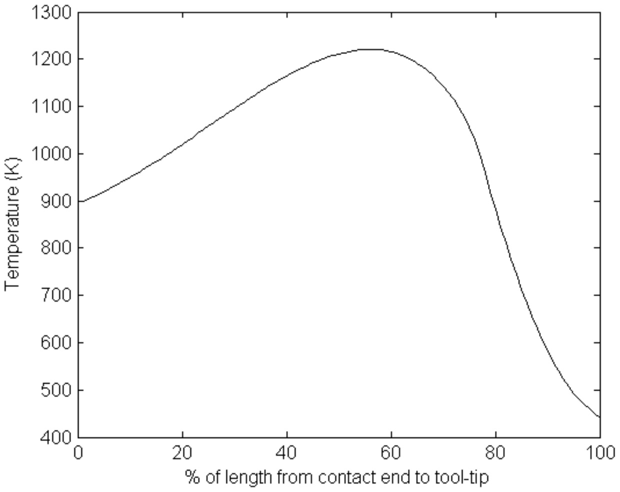

Figure 4.9 – Temperature rise on the interface c-t, chip side for AISI O2.

When considering the whole chip and the sum of the contributions, the results can be seen in figure 4.10:

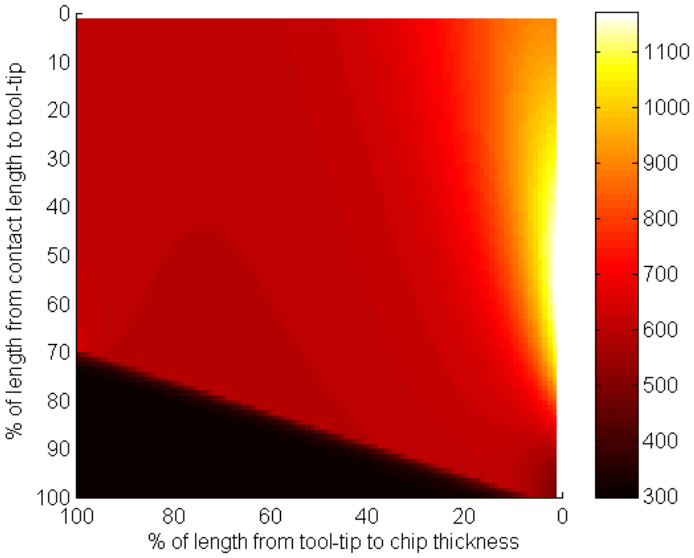

Figure 4.10 – Temperature rise on the chip for AISI O2.

In conclusion, for the chip, with these parameters, the model pointed out two hotspots a less heated one near the end of the shear zone and a much stronger one due to friction at the interface chip-tool, although affecting a much smaller volume of the chip when compared to the shear heat source.

4.4. Temperature rise in the tool

Inputting in the model the AISI O2 material parameters, the values for the heat partition equation of the tool (see equation (3.22)) taken from Komanduri and Hou’s work [20], the values for the heat partition equation due to induction on the rake face (see equation (3.22)) taken from Komanduri and Hou’s work [21], and assuming the tool to be perfectly sharp (no flank due to wear) the temperature rise in the tool was calculated. The tool was considered to be a tungsten carbide material, this only influences the model with its thermal conductivity parameter (λ_t), which was considered to be 100 $Wm^{-1} K^{-1}$ [26].

The temperature rise in the interface chip-tool (c-t), on the tool side, due to friction is shown in figure 4.11:

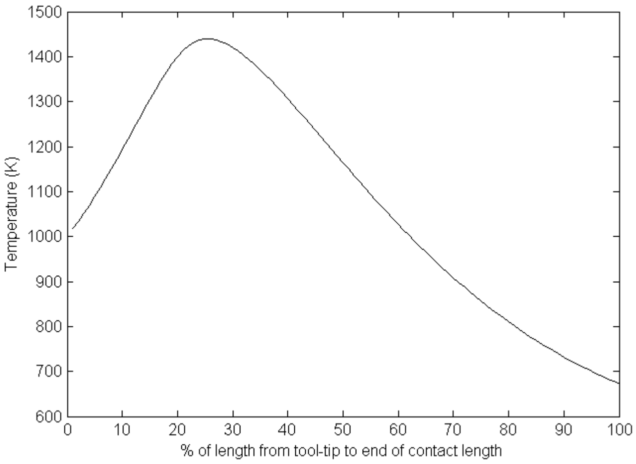

Figure 4.11 – Temperature rise on the interface c-t, tool side, due to the friction heat source for AISI O2.

Once again when analyzing the temperature rise due to friction, the friction model influences it heavily. The temperature rises steadily in the sticking zone and then drops gradually to a new temperature rise minimum.

Since the value of the temperature rise due to friction in the tool side (see figure 4.11) was found to be much higher than that of the temperature rise in the chip side (see figure 4.7) it is clear the equation of the heat partition needs adjusting so that the total temperature in the interface chip-tool shows that same temperature on the chip side and on the tool side.

When considering a significant part of the tool (the length of the chip thickness), the results due to the friction heat source are depicted in figure 4.12:

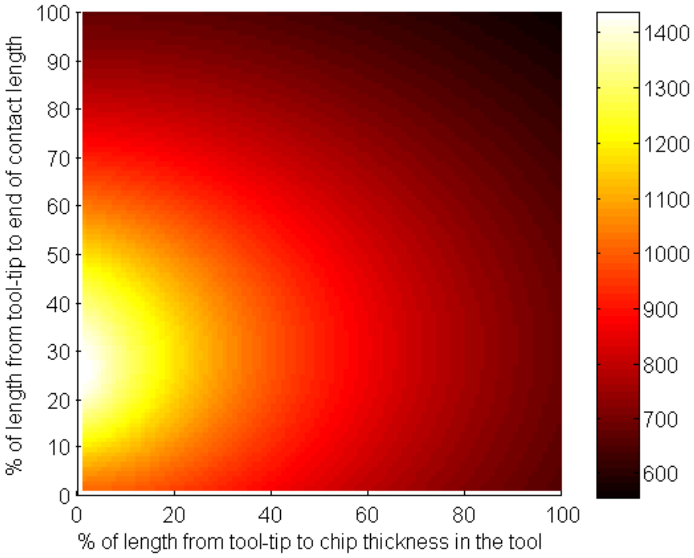

Figure 4.12 – Temperature rise on the tool due to the friction heat source for AISI O2.

As referred to in chapter 3, the temperature rise in the interface chip-tool, on the tool side, is influenced by to the heat induction from the shear heat source. This effect is shown in figure 4.13:

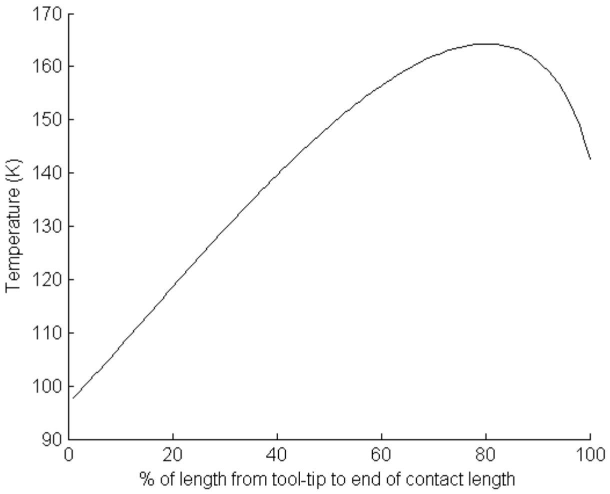

Figure 4.13 – Temperature rise on the interface c-t, tool side, due to induction from the shear heat source for AISI O2.

The temperature rise in the tool due to induction on the rake face gradually increases until a certain point. This should be related to the material crossing the shear zone and carrying heat previously to the contact with the chip-tool interface.

When considering a significant part of the tool (the length of the chip thickness), the results due to induction on the rake face can be seen in figure 4.14:

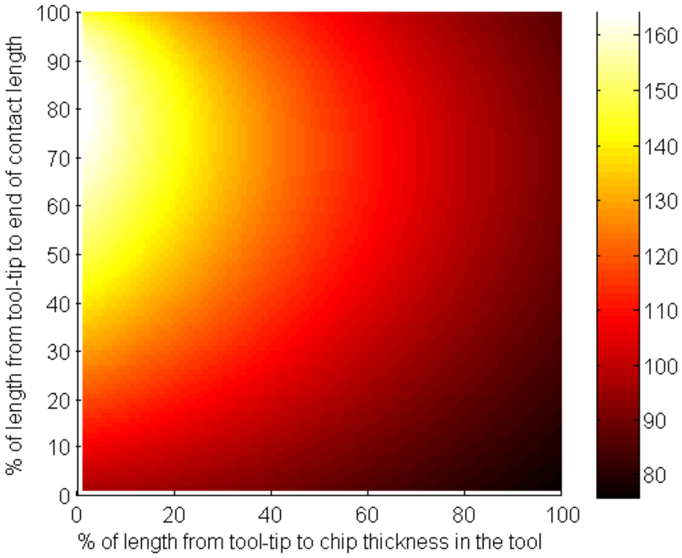

Figure 4.14 – Temperature rise on the tool due to induction on the rake face for AISI O2.

Although the temperature rise on the tool due to induction in the rake face is not as significant as due to other contributions it contributes for an overall more robust model.

When considering the sum of the contributions (see equation (3.44)), the results were printed in figure 4.15:

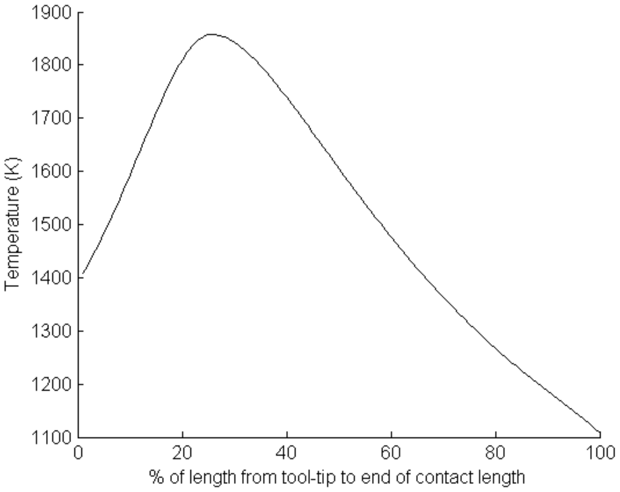

Figure 4.15 – Temperature rise on the interface c-t, chip side for AISI O2.

When considering a significant part of the tool (the length of the chip thickness) and the sum of the contributions, the results were printed in figure 4.16:

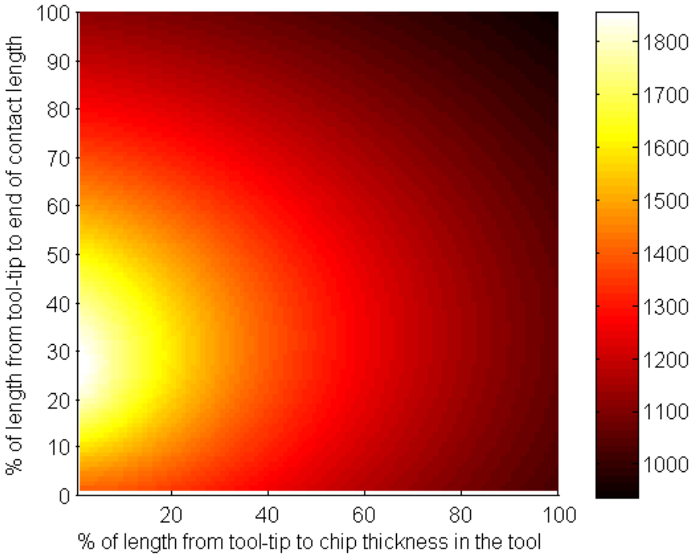

Figure 4.16 – Temperature rise on the tool for AISI O2.

In conclusion, for the tool, with these parameters, the model pointed out a hotspot near the end of the sticking zone and beginning of the sliding zone related mostly to the friction heat source. But even though the contribution from the induction on the rake face is much smaller it is still relevant reaching a temperature rise of around 160K at the maximum point.

4.5. Temperature rise in the chip and tool after interface chip-tool balancing

The temperatures in the interface chip-tool should be similar whether the chip or the tool side is considered. Since this was not found to be the case a balancing of temperatures was needed. The balancing of temperatures on the chip side with temperatures on the tool side is a multiple-variable optimization problem. In order to solve this, as shown before, heat partition equations were used. To simplify the calculations and solve this problem the heat partition ratios at the interfaces are calculated by matching average temperatures at those interfaces. Since there are virtually countless solutions for the ratios involved in the heat partition, an additional consideration was made that the maximum temperatures should match. By iteration the solution for this problem, with these constraints can be characterized by the ratios for the heat partition shown in table 4.3:

Table 4.3 Ratios for the heat partition in chip-tool interface

	Values from Komanduri and Hou [20]	**Values for balancing**
$\mathbf{B_{chip}}$	0.62	0.77
$\mathbf{\Delta B_1}$	0.35	0.21

$\mathbf{m}_1$	0.24	0.24
$\mathbf{C}_1$	2	2
$\mathbf{k}_1$	16	16
$\mathbf{B}_{\mathbf{ind}}$	1	1
$\Delta \mathbf{B}_i$	0.8	0.8
$\mathbf{m}_\mathbf{i}$	0.3	0.3
$\mathbf{C}_\mathbf{i}$	0.2	0.2
$\mathbf{k}_\mathbf{i}$	4	4

When the values for the heat partition ratios from Komanduri and Hou [20] were used, the results can be seen in figure 4.17:

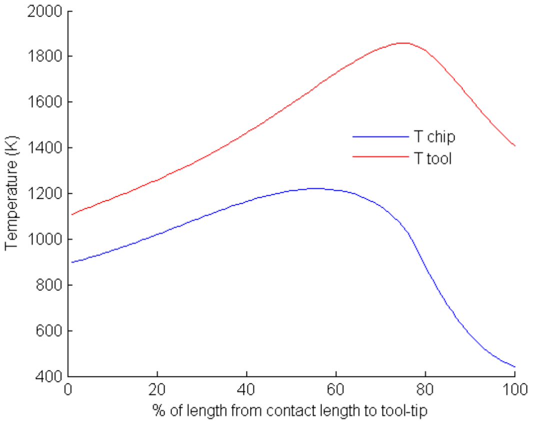

Figure 4.17 – Temperature in the chip and tool with heat partition ratios from Komanduri and Hou for AISI O2.

There is no match between the two curves and the overall difference of the averaging temperature on the two sides of the interface is very significant.

For the values found by an iterative process for the heat partition ratios the result can be seen in figure 4.18:

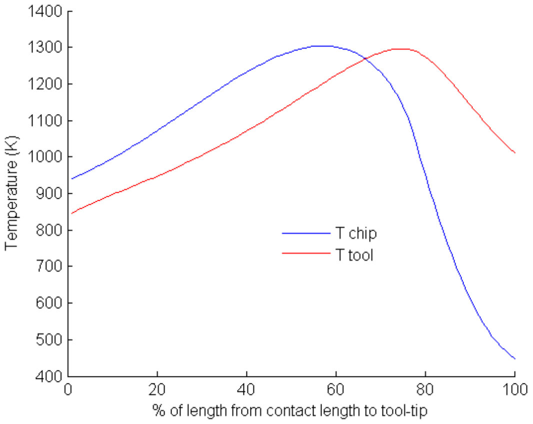

Figure 4.18 – Temperature in the chip and tool with heat partition ratios for balancing for AISI O2.

Although a complete match between the two curves was not found (the two curves are calculated by two different processes and came from two different models making the complete matching of the two curves impossible with the heat partition equations as they are), the maximum temperature on both is around the same and the difference between averaging temperatures of chip and tool is much lower.

When considering the whole chip and the sum of the contributions, the results using the new heart partition ratios for balancing are depicted in figure 4.19:

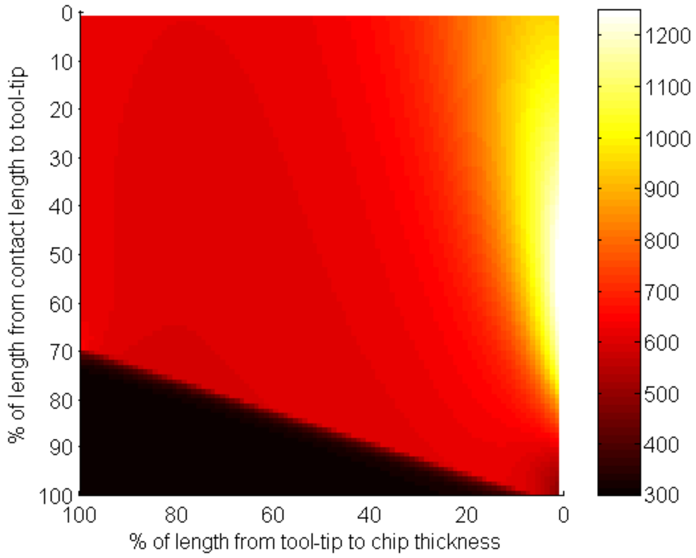

Figure 4.19 – Temperature rise on the chip after balancing for AISI O2.

When considering a significant part of the tool (the length of the chip thickness) and the sum of the contributions, the results using the new heat partition ratios for balancing can be seen in figure 4.20:

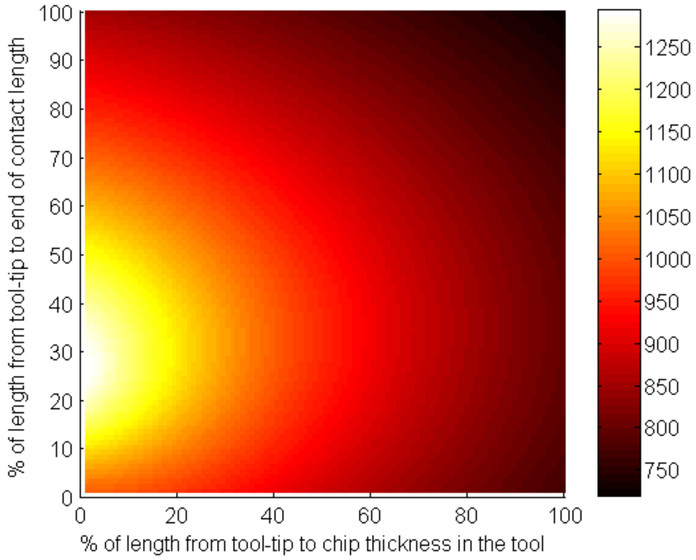

Figure 4.20 – Temperature rise on the tool for AISI O2.

In conclusion, after the balancing the maximum temperature on the chip rose slightly while the maximum temperature on the tool decreased significantly, this achieved an overall more uniform temperature rise process with the temperatures on the chip being on the same range of values as the temperatures on the tool.

4.6. Temperature rise in the tool and workpiece with a wear flank

When a flank face was considered, with a value of 0.3mm, some contributions were added to the temperature rise in the tool, namely the contribution of the induction on the flank face and the rubbing heat source.

With the introduction of a new face of contact a new area for heat partition is also added. A balancing of temperatures in the interface between the flank face of the tool and the area in contact of the work piece was also done, following the same criteria as before, the solution for this problem can be characterized by the ratios for the heat partition shown in table 4.4:

Table 4.4 Ratios for the heat partition in tool-work piece interface

	Values for balancing
$\mathbf{B_{work}}$	0.49
$\mathbf{\Delta B_2}$	0.22
$\mathbf{m_2}$	0.24
$\mathbf{C_2}$	4
$\mathbf{K_2}$	0.8

With these values for the ratios, the results for the temperatures in the interface on the tool side and work piece side can be seen in figure 4.21:

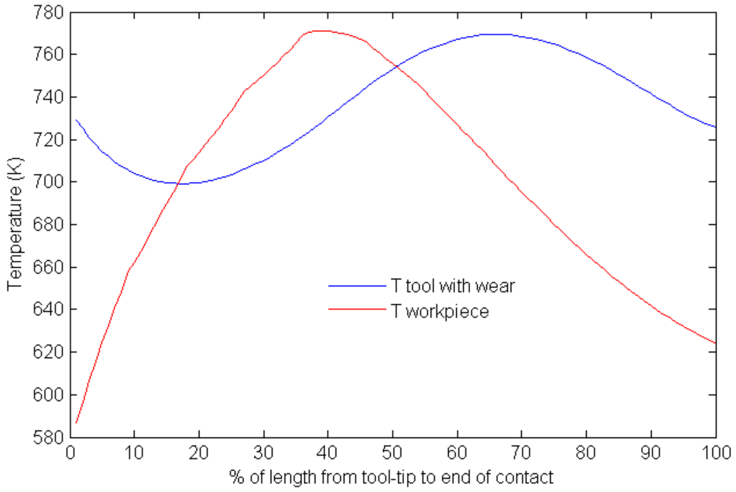

Figure 4.21 – Temperatures in the tool and work piece with heat partition ratios for balancing for AISI O2.

The temperature in the tool with a wear flank shown in figure 4.21 can be decomposed in its various contributions. These can be seen in figure 4.22:

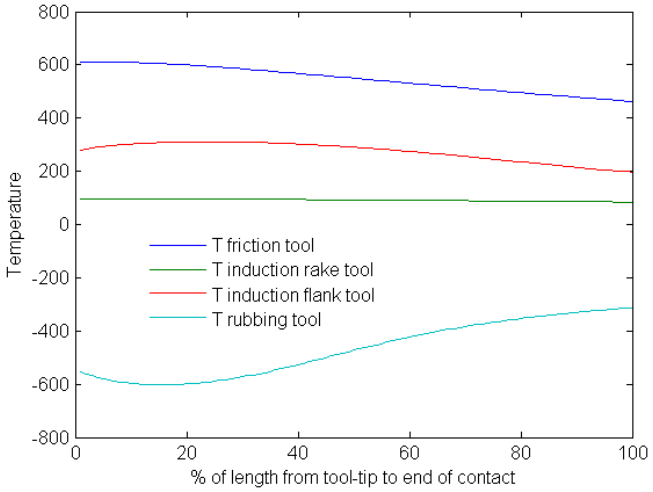

Figure 4.22 – Temperatures in the tool balanced for AISI O2.

In general the temperatures do not vary much along the flank face, which was expected since it's such a short length, nevertheless the rubbing heat source shows a different behavior with high negative values which are explained by the heat partition ratios, since to achieve an overall balance of temperatures in the flank face (in the tool and work piece sides) it seems the heat generated due to rubbing in the tool flows into the work piece and not the tool.

On the other hand, the temperature in the work piece wear flank shown in figure 4.21 can be decomposed in the contributions seen in figure 4.23:

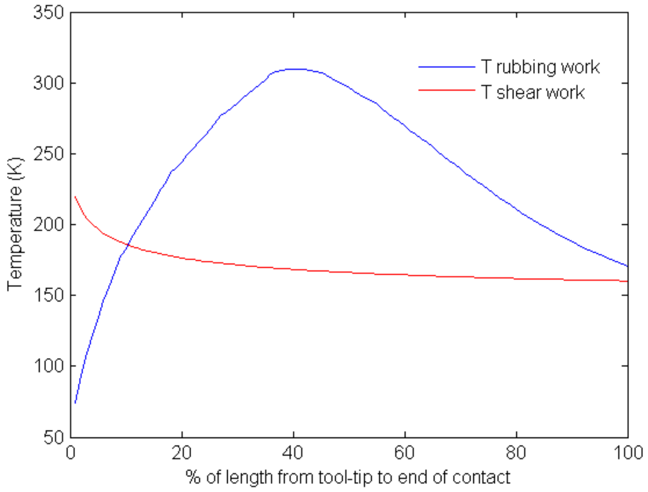

Figure 4.23 – Temperatures in the work piece balanced for AISI O2.

As was expected the temperature in the flank face due to shear is higher at the tool-tip since it is closer to the heat source but does not decreases too much due to the short length of the flank face. The temperature rise due to rubbing in the work piece rises until the critical plastic flow point and then decreases as was also expected. It should be noted that it was observed that the temperature rise due to rubbing whether on the tool or the work piece is very affected by the variation of the heat partition ratios.

When considering a significant part of the work piece (around 0.1mm) under the flank face and the sum of the contributions, the results are shown in figure 4.24:

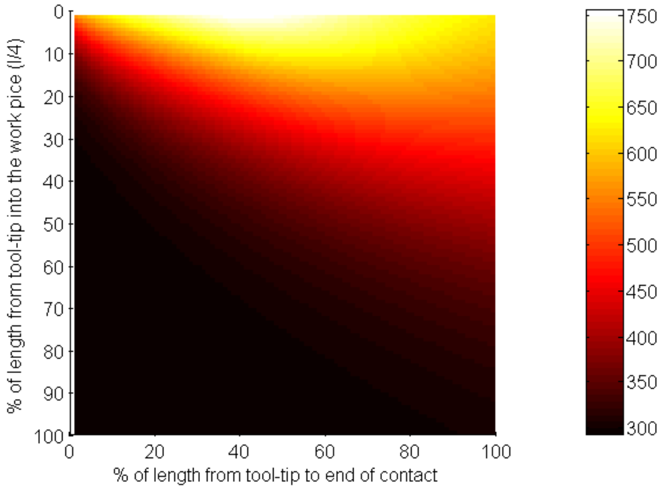

Figure 4.24 – Temperature rise on the work piece for AISI O2.

5

CONCLUSIONS

This chapter presents the main conclusions resulting of this work as well as suggestions for future work in this field.

5.1. Conclusions

The work presented in chapter 2 solidifies a good understanding of the fundamentals in the thermo-mechanical process involved in orthogonal metal cutting, synthesizing the information researched into a good base to be used as groundwork for future investigations.

The models proposed in chapter 3 succeed in compiling the analytical models into numerical ones to create a comprehensive model that is sensitive not only to different parameters and their coupling effects, but also encompasses all the different contributions to the temperature rises as was the objective. This was obtained by joining the different models from the different areas of study involved in orthogonal cutting, into a single model. It should also be noted the fact that even though each contribution implies its own system of axis, an effort was made to obtain a global model which translates all the temperature rises into the same system of axis for a much easier examination of the results.

The results in chapter 4 show the expected behavior and are portrayed in an intuitive manner, nevertheless, they show a strong dependence on the heat partition ratios which is the point where further investigation should be developed in order to provide a more robust model. Some of the relevant conclusions are:

- The results of the temperature rise in the chip showed that a good estimation of the chip’s mean temperature in the shear zone, used to determine the constitutive state of the material, is paramount for a viable calculation of the temperatures involved in orthogonal cutting.
- The temperature of the chip in the shear plane is not affected by the temperature rise due to friction. This is an important conclusion since it means that the temperature rise in the shear plane determined by the global model represents the effect due uniquely to shear.
- The numerical model showed to be sensible to the materials used and not only to the cutting parameters. The use of this model is therefore a valuable tool not only to a specific studied material but to the material relevant to a possible future research using any other metal with the same type of elastic-viscoplastic behavior as described before.
- The friction model used has a high degree of influence in the temperature, justifying its use and giving answer to some experimentally observed issues, as is the case of adhesion, or the case of progressive and gradual wear of the tools rake face.
- The wear model used in this work has a heavy influence, not only in the value of the temperature rise of the process, but in the way the model translates the process itself,

since it adds a flank face. The results observed after this addition to the model, points to the fact that a worn tool produces a much higher temperatures in the orthogonal cutting process.

- The results of the temperature in the tool and work piece with the variation of heat partition ratios in the interfaces considered, point to high variability of the behavior of the various heat interactions involved, especially due to rubbing. These ratios, or ultimately the heat partition equations, need further research for a deeper conclusion in this specific area.
- The model also determined the heat affected depth which could be an relevant factor when considering surface integrity of machined surfaces.

5.2. Suggestions for future work

Due to the complexity of this research and limited by its time frame, experimental work to further validate this thesis was not possible. Nevertheless, such important complementing work is already being made by another colleague and it will help to determine better heat partition ratios and overall validation of the model.

In the future, this area should evolve to include research in other types of chip cutting as well as include other considerations, such as nose radius on the tool-tip or chip-breakers, which will naturally lead to a three dimensional environment. Once this is achieved, a look into the issues in high speed machining will possibly be interesting.

BIBLIOGRAPHY

[1] T. Ozel and E. Zeren, "Determination of work material flow stress and friction for FEA of machining using orthogonal cutting tests," *Journal of Materials Processing Technology,* vol. 153, pp. 1019-1025, Nov 10 2004.

[2] P. L. B. Oxley, *The mechanics of machining : an analytical approach to assessing machinability*. Chichester England New York: E. Horwood ; Halsted Press, 1989.

[3] G. R. Johnson and W. H. Cook, "A constitutive model and data for metals subjected to large strains, high strain rates and high temperatures," in *Proceedings of the 7th International Symposium on Ballistics*, 1983, pp. 541-547.

[4] M. Sima and T. Ozel, "Modified material constitutive models for serrated chip formation simulations and experimental validation in machining of titanium alloy Ti-6Al-4V," *International Journal of Machine Tools & Manufacture,* vol. 50, pp. 943-960, Nov 2010.

[5] M. Weber, T. Hochrainer, P. Gumbsch, H. Autenrieth, L. Delonnoy, V. Schulze*, et al.*, "Investigation of size-effects in machining with geometrically defined cutting edges," *Machining Science and Technology,* vol. 11, pp. 447-473, Oct-Dec 2007.

[6] N. Fang, I. S. Jawahir, and P. L. B. Oxley, "A universal slip-line model with non-unique solutions for machining with curled chip formation and a restricted contact tool," *International Journal of Mechanical Sciences,* vol. 43, pp. 557-580, Feb 2001.

[7] G. Boothroyd, *Fundamentals of Metal Machining and Machine Tools, Second Edition*: Taylor & Francis, 1988.

[8] P. J. Arrazola, T. Oezel, D. Umbrello, M. Davies, and I. S. Jawahir, "Recent advances in modelling of metal machining processes," *Cirp Annals-Manufacturing Technology,* vol. 62, pp. 695-718, 2013 2013.

[9] S. Kato, K. Yamaguchi, and M. Yamada, "Stress Distribution at the Interface Between Tool and Chip in Machining," *Journal of Manufacturing Science and Engineering,* vol. 94, pp. 683-689, 1972.

[10] E. Ozlu, E. Budak, and A. Molinari, "Analytical and experimental investigation of rake contact and friction behavior in metal cutting," *International Journal of Machine Tools & Manufacture,* vol. 49, pp. 865-875, Sep 2009.

[11] S. Bahi, M. Nouari, A. Moufki, M. El Mansori, and A. Molinari, "A new friction law for sticking and sliding contacts in machining," *Tribology International,* vol. 44, pp. 764-771, Jul 2011.

[12] T. Ozel and T. Altan, "Determination of workpiece flow stress and friction at the chip-tool contact for high-speed cutting," *International Journal of Machine Tools & Manufacture,* vol. 40, pp. 133-152, Jan 2000.

[13] A. Moufki, A. Molinari, and D. Dudzinski, "Modelling of orthogonal cutting with a temperature dependent friction law," *Journal of the Mechanics and Physics of Solids,* vol. 46, pp. 2103-2138, Oct 1998.

[14] Y. Karpat and T. Ozel, "Predictive analytical and thermal modeling of orthogonal cutting process - Part I: Predictions of tool forces, stresses, and temperature distributions," *Journal of Manufacturing Science and Engineering-Transactions of the Asme,* vol. 128, pp. 435-444, May 2006.

[15] Y. Huang and S. Y. Liang, "Modelling of the cutting temperature distribution under the tool flank wear effect," *Proceedings of the Institution of Mechanical Engineers Part C-Journal of Mechanical Engineering Science,* vol. 217, pp. 1195-1208, 2003 2003.

[16] Y. Karpat and T. Ozel, "Predictive analvtical and thermal modeling of orthogonal cutting process - Part II: Effect of tool flank wear on tool forces, stresses, and temperature distributions," *Journal of Manufacturing Science and Engineering-Transactions of the Asme,* vol. 128, pp. 445-453, May 2006.

[17] Y. Huang and S. Y. Liang, "Modeling of cutting forces under hard turning conditions considering tool wear effect," *Journal of Manufacturing Science and Engineering-Transactions of the Asme,* vol. 127, pp. 262-270, May 2005.

[18] N. A. Abukhshim, P. T. Mativenga, and M. A. Sheikh, "Heat generation and temperature prediction in metal cutting: A review and implications for high speed machining," *International Journal of Machine Tools & Manufacture,* vol. 46, pp. 782-800, Jun 2006.

[19] R. Komanduri and Z. B. Hou, "Thermal modeling of the metal cutting process - Part I - Temperature rise distribution due to shear plane heat source," *International Journal of Mechanical Sciences,* vol. 42, pp. 1715-1752, Sep 2000.

[20] R. Komanduri and Z. B. Hou, "Thermal modeling of the metal cutting process - Part II: temperature rise distribution due to frictional heat source at the tool-chip interface," *International Journal of Mechanical Sciences,* vol. 43, pp. 57-88, Jan 2001.

[21] R. Komanduri and Z. B. Hou, "Thermal modeling of the metal cutting process - Part III: temperature rise distribution due to the combined effects of shear plane heat source and the tool-chip interface frictional heat source," *International Journal of Mechanical Sciences,* vol. 43, pp. 89-107, Jan 2001.

[22] E. W. Weisstein. *"Bessel Function of the Second Kind."*. Available: http://mathworld.wolfram.com/BesselFunctionoftheSecondKind.html, accessed on 23-06-2014.

[23] E. W. Weisstein. *"Modified Bessel Function of the Second Kind."*. Available: http://mathworld.wolfram.com/ModifiedBesselFunctionoftheSecondKind.html, accessed on 23-06-2014.

[24] J. P. Davim, *Machining: Fundamentals and Recent Advances*: Springer, 2008.

[25] M. Ravne. *"Alphabetical Steel Index"*. Available: http://www.metalravne.com/selector/html/steel_index.html, accessed on 09-07-2014.

[26] CoorsTek. *"Tungsten Carbide Material Properties"*. Available: http://www.coorstek.com/materials/ceramics/carbides_WC.php, accessed on 15-07-2014.

APPENDIX A

The need for a local friction coefficient expression led the following formulation.

Considering (see figure 2.4):

$$\tan\lambda = \frac{F_{frict}}{F_{Normal}} \tag{A1}$$

Since the frictional force is known:

$$\begin{aligned} F_{Frict} &= \int_0^{l_P} \tau_S \cdot W\,dx + \int_{l_P}^{l_C} \tau_S \cdot \left(1 - \frac{x - l_P}{l_c}\right)^{\psi} \cdot W\,dx \\ &= \mu_{local} \cdot P_0 \cdot W \cdot \left(1 - \frac{l_P}{l_c}\right)^{\psi} \cdot \left(l_P + \frac{l_C - l_P}{\psi + 1}\right) \end{aligned} \tag{3.14}$$

As well as the normal force:

$$F_{Normal} = \int_0^{l_C} P(x)\,dx = \int_0^{l_C} P_0 \left(1 - \frac{x}{l_c}\right)^{\psi} \cdot W\,dx = P_0 \frac{W \cdot l_C}{\psi + 1} \tag{3.13}$$

$\tan\lambda$ then becomes:

$$\tan\lambda = \frac{\mu_{local} \cdot P_0 \cdot W \cdot \left(1 - \frac{l_P}{l_c}\right)^{\psi} \cdot \left(l_P + \frac{l_C - l_P}{\psi + 1}\right)}{P_0 \frac{W \cdot l_C}{\psi + 1}} \tag{A2}$$

Rearranging the expression:

$$\mu_{local} = \frac{\tan\lambda \cdot l_c}{\frac{(l_c - l_p)^{\psi}}{{l_c}^{\psi}} \cdot \left(l_p + \frac{l_c - l_p}{\psi + 1}\right) \cdot (\psi + 1)} \tag{A3}$$

Given that:

$$(l_c - l_p)^{\psi} = {l_c}^{\psi} \cdot \left(1 - \frac{l_p}{l_c}\right)^{\psi} \leftrightarrow \frac{\left(l_c - l_p\right)^{\psi}}{{l_c}^{\psi}} = \left(1 - \frac{l_p}{l_c}\right)^{\psi} \tag{A4}$$

The local friction coefficient can finally be given by:

$$\mu_{local} = \frac{\tan\lambda \cdot {l_c}^{\psi+1}}{(l_c + l_p \cdot \psi) \cdot (l_c - l_p)^{\psi}} \tag{3.11}$$

Which then leads to the need of knowing the length of the sticking zone, l_p.

Considering that at l_p the shear stress on the rake face is equal to the shear yield stress of the material:

$$\tau_c = \mu_{local} \cdot P_0 \left(1 - \frac{x}{l_c}\right)^{\psi} \quad \text{A5}$$

With the normal stress exerted on the rake face at the tool tip:

$$P_0 = 4 \cdot \frac{\psi + 1}{\psi + 2} \cdot \frac{\cos^2 \lambda}{\sin 2\theta} \cdot \tau_S \quad (2.25)$$

And the equation A4, the equation A5 can be rearranged to become:

$$l_p = \left(4 \cdot \frac{\psi + 1}{\psi + 2} \cdot \frac{\cos^2 \lambda}{\sin 2\theta} \cdot \tan \lambda \cdot \frac{\tau_S}{\tau_C} \cdot l_c - l_c\right) \frac{1}{\psi} \quad (3.12)$$

APPENDIX B

The need for a length of the wear flank until critical plastic flow point expression led the following formulation.

Since at the critical plastic flow point $\tau_{rubbing} = \tau_s$:

$$\tau_s = \mu \cdot \sigma_0 \cdot \left(\frac{\mathrm{l}_f - \mathrm{l}_{fc}}{\mathrm{l}_f}\right)^2 \tag{3.30}$$

Because σ_0 can be equated to:

$$\sigma_0 = \tau_s \left[1 + \frac{\pi}{2} - 2\rho - 2\Phi + 2\gamma + \sin(2\gamma - 2\Phi)\right] \tag{2.32}$$

Where due to low plastic deformation, $\rho = n_p = 0$ which implies $\gamma = \Phi$ (see equation 2.33), and so:

$$\sigma_0 = \tau_s \cdot \left(1 + \frac{\pi}{2}\right) \qquad \text{B1}$$

Rearranging the expressions B1 and (3.30), l_{fc} can be given by:

$$\mathrm{l}_{fc} = \mathrm{l}_f \cdot \left(1 - \sqrt{\frac{1}{1 + \frac{\pi}{2}}}\right) \tag{3.34}$$

APPENDIX C

C.3. Booting program

```
        pedir={'Velocidade de Corte (m/s):','Largura de corte (m):','Espessura da apara antes da
deformação (m):','Ângulo de ataque (grau):','Condição de maquinagem (seco/óleo de
corte):','Temperatura ambiente (K):'};
        valorespadrao={'120/60','2.5e-3','0.25e-3','5','2','293'};
        titulodadialog='Valores experimentais';
        num_lines=1;
        resposta = inputdlg(pedir,titulodadialog,num_lines,valorespadrao,'on');
        Vc = str2num(resposta{1});
        W = str2num(resposta{2});
        tu = str2num(resposta{3});
        alpha = str2num(resposta{4})*pi/180;
        xi = str2num(resposta{5});
        Tamb = str2num(resposta{6});
        pedir2={'Tensão de cedencia a zero Kelvin (Pa):','m parâmetro do modelo JC:','n parâmetro
do modelo JC:','Taxa de extensão critica (s^-1):',...
          'Entalpia de activação livre (J s):','athermal flow stress inicial (Pa):','k Coeficiente de
endurecimento (Pa):','r Coeficiente de encruamento:',...
          'upsilon A plastic strain rate pode ser adaptada ao material por este parametro
(K):','d_upsilon A plastic strain rate pode ser adaptada ao material por este parametro (K):',...
          'Temperatura de fusão (K):','eta A inclinação da descida do flow stress é ajustada por este
parametro:','zeta A inclinação da descida do flow stress é ajustada por este parametro:',...
          'Condutividade térmica (W m^-1 K^-1):'};
        %AISI O2
        valorespadrao2={'1550e6','3.23','0.57','1.75e7',...
          '1.82e-19','920e6','504e6','0.14',...
          '540','100',...
          '1723','2','11',...
          '46'};
        pedir3={'Módulo de Young a 273K (Pa):','e1 Para calcular o modulo de Young (Pa K^-1):',...
          'e2 Para calcular o modulo de Young (Pa K^-2):','densidade(kg /m^3):','Coeficiente de
Poisson a 273K:','difnu Para calcular o coeficiente de Poisson (K^-1):',...
          'Calor especifico a pressão constante(J kg^-1 K^-1):','Constante de Boltzmann (J K^-
1):','Difusividade térmica (m^2/s)'};
        valorespadrao3={'2.1e11','-52e6',...
          '-4.7e4','7850','0.283','4e-5',...
          '460','1.38e-23','8.308e-6'};
        %AISI 1045
        % valorespadrao2={'2000e6','1.78','0.5','4.41e7',...
        %    '1.03e-19','330e6','435e6','0.22',...
        %    '560','90',...
        %    '1793','2','9',...
        %    '50'};
        % pedir3={'Módulo de Young a 273K (Pa):','e1 Para calcular o modulo de Young (Pa K^-
1):',...
```

```
%     'e2 Para calcular o modulo de Young (Pa K^-2):','densidade(kg /m^3):','Coeficiente de Poisson a 273K:','difnu Para calcular o coeficiente de Poisson (K^-1):',...
%     'Calor especifico a pressão constante(J kg^-1 K^-1):','Constante de Boltzmann (J K^-1):','Difusividade térmica (m^2/s)'};
% valorespadrao3={'2.1e11','-52e6',...
%     '-4.7e4','7850','0.283','4e-5',...
%     '460','1.38e-23','4.19e-6'};
%
titulodadialog2='Parâmetos constitutivos do material da peça';
num_lines2=1;
resposta2 = inputdlg(pedir2,titulodadialog2,num_lines2,valorespadrao2,'on');
titulodadialog3='Parâmetos constitutivos do material da peça (cont.)';
num_lines3=1;
resposta3 = inputdlg(pedir3,titulodadialog3,num_lines3,valorespadrao3,'on');
sigma_ast_0= str2num(resposta2{1});
m= str2num(resposta2{2});
n= str2num(resposta2{3});
epsilon_pt_0= str2num(resposta2{4});
difGO= str2num(resposta2{5});
sigma_GO= str2num(resposta2{6});
k= str2num(resposta2{7});
r= str2num(resposta2{8});
upsilon= str2num(resposta2{9});
d_upsilon= str2num(resposta2{10});
Tmelt= str2num(resposta2{11});
eta= str2num(resposta2{12});
zeta= str2num(resposta2{13});
lambda_c= str2num(resposta2{14});
E273= str2num(resposta3{1});
e1= str2num(resposta3{2});
e2= str2num(resposta3{3});
ro= str2num(resposta3{4});
nu273= str2num(resposta3{5});
difnu= str2num(resposta3{6});
cp= str2num(resposta3{7});
Kb= str2num(resposta3{8});
ac= str2num(resposta3{9});
%
lambda=atan(0.6); % Eq.(2.13)
C=5;
% Bchip=0.620; %Valores retirados do trabalho de Komanduri part II
% difB1=0.35;
% m1=0.24;
% C1=2;
% k1=16;
%
Bchip=0.77; % Bom balanceamento
difB1=0.21;
m1=0.24;
C1=2;
k1=16;
%
phi=pi/4+(alpha-lambda)/2; % Eq.(2.12)
theta=atan (1+2*(pi/4-phi)-(C*r)); % Eq.(2.22)
l=tu/sin (phi); % Eq.(2.17)
```

```
lc=(xi+2)/2*(sin (theta)/(sin (phi)*cos (lambda))*tu); % Eq.(2.26)
tc=l*cos(phi-alpha); % FALTA
Vs=cos (alpha)/cos(phi-alpha)*Vc; % Eq.(2.9)
Vchip=sin (phi)/cos(phi-alpha)*Vc; % Eq.(2.8)
gama_pt_AB=C*Vs/l; % Eq.(2.16)
epsilon_pt_AB=gama_pt_AB/sqrt(3); % Eq.(2.19)
Tt_ep_AB=upsilon-d_upsilon*log (1+epsilon_pt_AB/epsilon_pt_0); % Eq.(2.6)
gama_AB=cos (alpha)/(2*sin (phi)*cos (phi-alpha)); % Eq.(2.15)
epsilon_AB=gama_AB/sqrt(3); % Eq.(2.18)
E_OK=E273+e1*(0-273)+e2*(0-273)^2; % Eq.(2.4)
nu_OK=nu273+difnu*(0-273); % Eq.(2.4)
G_OK=E_OK/(2*(1+nu_OK)); % Eq.(2.4)
Tdislocations=difGO/(Kb*log (epsilon_pt_0/epsilon_pt_AB)); % Eq.(2.2)
%

T_AB=Tamb;%average temperature along the primary shear plane OA.
erro=1000;
i=0;
while erro > 10;
   i=i+1;
 if     T_AB<=Tt_ep_AB; % Eq.(2.5)
     g_T_Tt=1; % Eq.(2.5)
 else
     g_T_Tt=(1-((T_AB-Tt_ep_AB)/(Tmelt-Tt_ep_AB))^eta)^zeta; % Eq.(2.5)
 end
E_T_AB=E273+e1*(T_AB-273)+e2*(T_AB-273)^2; % Eq.(2.4)
nu_TAB=nu273+difnu*(T_AB-273); % Eq.(2.4)
G_T_AB=E_T_AB/(2*(1+nu_TAB)); % Eq.(2.4)
E_Tamb=E273+e1*(Tamb-273)+e2*(Tamb-273)^2; % Eq.(2.4)
nu_Tamb=nu273+difnu*(Tamb-273); % Eq.(2.4)
G_Tamb=E_Tamb/(2*(1+nu_Tamb)); % Eq.(2.4)
sigma_AB=sigma_ast_0*(1-(T_AB/Tdislocations)^n)^m+(sigma_GO+k*epsilon_AB^r)*G_T_AB/G_OK* g_T_Tt; % Eq.(2.7)
sigma_ced=sigma_ast_0*(1-(Tamb/Tdislocations)^n)^m+(sigma_GO)*G_Tamb/G_OK; % Eq.(2.7)
tau_s=sigma_AB/sqrt(3); % Eq.(2.20)
tau_c=sigma_ced/sqrt(3); % Eq.(2.21)
P0=4*(xi+1)/(xi+2)*((cos (lambda)*cos (lambda))/(sin (2*theta)))*tau_s; % Eq.(2.25)
F_Normal=P0*W*lc/(xi+1); % Eq.(3.13)
F_s=W*tu/sin (phi)*tau_s; % Eq.(3.15)
R=F_s/(cos (theta)); % Eq.(3.32)
q_shear=tau_s*Vs; % Eq.(3.4)
lp=1/xi*(4*(xi+1)/(xi+2)*cos (lambda)*cos (lambda)/sin (2*theta)*lc*tan (lambda)*tau_s/tau_c-lc); % Eq.(3.12)
frictcoef_local=lc^(xi+1)*tan (lambda)/((lp*xi+lc)*(lc-lp)^xi); % Eq.(3.11)
%Variáveis para execução do ciclo.
divisoesdazonadefric=11111; %Número de divisões da zona secundária (de fricção na interface f/a)
divisoesdex=100; %Número de pontos onde são calculadas as temperaturas
divisoesdel1=1111;
int_li0=0;
%Para o lado da chip:
fi=phi-alpha;
V=Vchip;
```

```
        for posicaodex=1:1:divisoesdex
        z=l*posicaodex/divisoesdex*cos(fi); %Posição da fonte na zona primária.
        x=l*posicaodex/divisoesdex*sin(fi);  %Posição da fonte na zona primária.
          for posicaoeml1=1:1:divisoesdel1
                        R01=sqrt((x-l*posicaoeml1/divisoesdel1*sin(fi))^2+(z-l*posicaoeml1/divisoesdel1*cos(fi))^2)*V/(2*ac); % Eq.(3.2)
                        R02=sqrt((x-l*posicaoeml1/divisoesdel1*sin(fi))^2+(z+l*posicaoeml1/divisoesdel1*cos(fi))^2)*V/(2*ac); % Eq.(3.3)
                        if R01==0
                        int_li0(posicaoeml1)=int_li0(posicaoeml1-1);
                         AUXsinal(posicaoeml1)=posicaoeml1;
                        else
                        bess1=besselk(0,R01); % Eq.(3.1)
                        bess2=besselk(0,R02); % Eq.(3.1)
                        int_li0(posicaoeml1)=exp(-1*(x-l*posicaoeml1/divisoesdel1*sin(fi))*V/(2*ac))*(bess1+bess2)*l/divisoesdel1; % Eq.(3.1)
                        end
          end
                                integralshear=sum(int_li0); % Eq.(3.13)

        % Tfriction chip
        z=l*sin(pi/2-(phi-alpha))*posicaodex/divisoesdex;
        x=lc-l*cos(pi/2-(phi-alpha))*posicaodex/divisoesdex;
        %
          for posicaonazonadefric=1:1:divisoesdazonadefric
                    xfrictchip=posicaonazonadefric/divisoesdazonadefric*lc;
                if xfrictchip<=lc-lp
                 Vchipss=Vchip; % Eq.(3.8)
                  tf1=frictcoef_local*P0*(xfrictchip/(lc-lp))^xi; % Eq.(3.10)
                else
                     Vchipss=Vchip*(1-(xfrictchip-(lc-lp))/lp)^2; % Eq.(3.8)
                    tf1=frictcoef_local*P0; % Eq.(3.10)
                end
                   q_friction=tf1*Vchipss; % Eq.(3.9)
                    B1chip=(Bchip-difB1)+2*difB1*((lc-xfrictchip)/lc)^m1+C1*difB1*((lc-xfrictchip)/lc)^k1; % Eq.(3.16)
                        R3=sqrt((x-lc*posicaonazonadefric/divisoesdazonadefric)^2+(z)^2)*V/(2*ac); % Eq.(3.6)
                        R4=sqrt((x-lc*posicaonazonadefric/divisoesdazonadefric)^2+(2*tc-z)^2)*V/(2*ac); % Eq.(3.7)
                        if R3==0
                        int_li1(posicaonazonadefric)=mean(int_li1);
                        else
                        bess41=besselk(0,R3); % Eq.(3.5)
                        bess42=besselk(0,R4); % Eq.(3.5)
                        int_li1(posicaonazonadefric)=q_friction*B1chip*exp(-1*(x-lc*posicaonazonadefric/divisoesdazonadefric)*V/(2*ac))*(bess41+bess42)*lc/divisoesdazonadefric; % Eq.(3.5)
                        end
          end
                                integralfriction_chip_OA=sum(int_li1); % Eq.(3.5)
         Tshear=(q_shear/(2*pi*lambda_c))*integralshear; % Eq.(3.1)
         Tshear_AB(posicaodex)=Tshear;
         %
```

```
   Tfriction_chip=(1/(pi*lambda_c))*integralfriction_chip_OA; % Eq.(3.5)
   Tfriction_chip_AB(posicaodex)=Tfriction_chip;
   Tfriction_chip_ABinvertido=fliplr(Tfriction_chip_AB);
  %

end
   TchipAB=Tfriction_chip_ABinvertido+Tshear_AB+Tamb;
T_AB2=mean(TchipAB);
    erro=abs(T_AB2-T_AB);
     T_AB=T_AB2;
    T(i)=T_AB;
end
figure
hold all
plot(TchipAB)
plot(Tshear_AB)
plot(Tfriction_chip_AB)
plot(T)
```

C.4. T chip program

```
divisoesdex=100; %divisões de x
divisoesdexi=100; %divisões de xi
divisoesdeyi=100; %divisões de yi
divisoesdel=11111;
divisoesdez=100;
int_li2=0;
int_li4=0;
% Bchip=0.620; %Valores retirados do trabalho de Komanduri part II
% difB1=0.35;
% m1=0.24;
% C1=2;
% k1=16;
Bchip=0.77; % Bom balanceamento
difB1=0.21;
m1=0.24;
C1=2;
k1=16;
Btool=1-Bchip;
% T shear chip
for posicaoemz=1:1:divisoesdez
        z=tc-tc*posicaoemz/divisoesdez;
        simulation=posicaoemz
for posicaodex=1:1:divisoesdex
%
% z=tc; %Zona de fricção
% x=lc-2*lc*posicaodex/divisoesdex;
%
% z=0;
x=l*sin(phi-alpha)-lc*posicaodex/divisoesdex; %Da ponta da ferramenta até ao final do contacto f/a
%
% z=l*posicaodex/divisoesdex*cos(fi);
% x=l*posicaodex/divisoesdex*sin(fi);
%
    for posicaoeml=1:1:divisoesdel
                            R21=sqrt((x-l*posicaoeml/divisoesdel*sin(phi-alpha))^2+(z-l*posicaoeml/divisoesdel*cos(phi-alpha))^2)*Vchip/(2*ac);
                            R22=sqrt((x-l*posicaoeml/divisoesdel*sin(phi-alpha))^2+(z+l*posicaoeml/divisoesdel*cos(phi-alpha))^2)*Vchip/(2*ac);
                            if R21==0
                            int_li2(posicaoeml)=mean(int_li2);
                             AUXsinal(posicaoeml)=posicaoeml;
                            else
                            bess21=besselk(0,R21);
                            bess22=besselk(0,R22);
%                               bess32=0;
                            int_li2(posicaoeml)=exp(-1*(x-l*posicaoeml/divisoesdel*sin(phi-alpha))*Vchip/(2*ac))*(bess21+bess22)*l/divisoesdel;
                            end
    end
                                                  integralshear=sum(int_li2);
   Tshear_chip=(q_shear/(2*pi*lambda_c))*integralshear;
```

```
   AUXTshear_chip(posicaodex)=Tshear_chip;
   AUXTshearinvertchip=fliplr(AUXTshear_chip); %Do final de contacto até à ponta da ferramenta.
end
AUXMatrizShear(posicaoemz,:)=AUXTshearinvertchip;
%T friction chip
        z=tc*posicaoemz/divisoesdez;
for posicaodex=1:1:divisoesdex
% z=0;
x=lc*posicaodex/divisoesdex; %Do final da zona de contacto até à ponta da ferramenta.
    for posicaonazonadefric=1:1:divisoesdazonadefric
                   xfrictchip=posicaonazonadefric/divisoesdazonadefric*lc;
            %%%%% Sticking and Sliding
               if xfrictchip<=lc-lp
                Vchipss=Vchip;
                Vchipss1(posicaonazonadefric)=Vchipss;
                  tf1=frictcoef_local*P0*(xfrictchip/(lc-lp))^xi;
                  tf11(posicaonazonadefric)=tf1;
               else
                     Vchipss=Vchip*(1-(xfrictchip-(lc-lp))/lp)^2;
                     Vchipss1(posicaonazonadefric)=Vchipss;
                    tf1=frictcoef_local*P0;
                     tf11(posicaonazonadefric)=tf1;
               end
                       q_friction=tf1*Vchipss;
                        B1chip=(Bchip-difB1)+2*difB1*((lc-xfrictchip)/lc)^m1+C1*difB1*((lc-
xfrictchip)/lc)^k1; %Cálculo da partilha de calor na interface apara/ferramenta.
                        AUXBb1(posicaonazonadefric)=B1chip;
                             R41=sqrt((x-
lc*posicaonazonadefric/divisoesdazonadefric)^2+(z)^2)*Vchipss/(2*ac);
                             R42=sqrt((x-lc*posicaonazonadefric/divisoesdazonadefric)^2+(2*tc-
z)^2)*Vchipss/(2*ac);
                             if R41==0
                             int_li4(posicaonazonadefric)=mean(int_li4);
                              AUXsinal(posicaonazonadefric)=posicaonazonadefric;
                             else
                             bess41=besselk(0,R41);
                             bess42=besselk(0,R42);
                             int_li4(posicaonazonadefric)=q_friction*B1chip*exp(-1*(x-
lc*posicaonazonadefric/divisoesdazonadefric)*Vchipss/(2*ac))*(bess41+bess42)*lc/divisoesdazonade
fric;
                             end
    end
                                                    integralfriction=sum(int_li4);
   Tfriction_chip=(1/(pi*lambda_c))*integralfriction;
   AUXTfriction_chip(posicaodex)=Tfriction_chip;
end
AUXMatrizFriction(posicaoemz,:)= AUXTfriction_chip;
end
AUXTchip=AUXMatrizShear+AUXMatrizFriction+Tamb;
```

C.5. T tool sharp program

```
lambda_t=100;
lf=0; %Sharp!
divisoesdexi=100; %divisões de xi
divisoesdeyi=100; %divisões de yi
divisoesdel1=11111;
divisoesdez=100;
%%%%%%%%%%%%%%%%%%%%%%%%%%
% Bchip=0.620; %Valores retirados do trabalho de Komanduri part II
% difB1=0.35; %Valores que obtêm uma curva para a partilha de calor aproximada na interface
% m1=0.24;
% C1=2;
% k1=16;
%%%%%%%%%%%%%%%%%%%%%%%%%%
Bind=1; %Valores retirados do trabalho de Komanduri part II
difBi=0.8; %Valores que obtêm uma curva para a partilha de calor aproximada na interface
mi=0.3;
Ci=0.2;
ki=4;
%%%%%%%%%%%%%%%%%%%%%%%%%%
Btool=1-Bchip;
F_Ts=R*sin(-phi+theta); %Eq. (3.31)
Pw=F_Ts*3/(W*lf); %Eq. (3.30)
%b=l3*(1-frictcoef2);
%lfc=lf*(1-lambda);
lfc=lf*(1-sqrt(1/(1+pi/2))); %Eq. (3.33)
%%% q induction na face RAKE da TOOL
%Para o lado da chip:
fi=phi-alpha;
V=Vchip;
int_li2=0;
for posicaoemx=1:1:divisoesdex
zperm1=tc; %A posição de z neste cálculo é permanentemente tc.
x=l*sin(fi)-lc*posicaodex/divisoesdex; %Da ponta da ferramenta até ao final do contacto f/a
  for posicaoeml1=1:1:divisoesdel1
                R21=sqrt((x-l*posicaoeml1/divisoesdel1*sin(fi))^2+(zperm1-
l*posicaoeml1/divisoesdel1*cos(fi))^2)*V/(2*ac);
                R22=sqrt((x-
l*posicaoeml1/divisoesdel1*sin(fi))^2+(zperm1+l*posicaoeml1/divisoesdel1*cos(fi))^2)*V/(2*ac);
                if R21==0
                int_li2(posicaoeml1)=mean(int_li2);
                 AUXsinal(posicaoeml1)=posicaoeml1;
                else
                bess21=besselk(0,R21);
                bess22=besselk(0,R22);
%                  bess32=0;
                int_li2(posicaoeml1)=exp(-1*(x-
l*posicaoeml1/divisoesdel1*sin(fi))*V/(2*ac))*(bess21+bess22)*l/divisoesdel1;
                end
  end
                             integralshear=sum(int_li2);
 Tshear_chip=(q_shear/(2*pi*lambda_c))*integralshear;
```

```
  AUXTshear_chip(posicaoemx)=Tshear_chip;
end
somatorioTshearchip=sum(AUXTshear_chip);
%
for posicaoemx=1:1:divisoesdex
x=posicaoemx/divisoesdex*lc; %Do final do contacto f/a até à ponta da ferramenta.
zperm2=0;  %A posição de z neste cálculo é permanentemente zero.
            for posicaoemxi=1:1:divisoesdexi
              xfrict=posicaoemxi/divisoesdexi*lc;
                     Btoolinduced=(Bind+difBi)-2*difBi*(xfrict/lc)^mi-Ci*difBi*(xfrict/lc)^ki;
%                    B1tool=(Btool+difB1)-2*difB1*(xfrict/lc)^m1-C1*difB1*(xfrict/lc)^k1;
%                    AUXBtool(posicaoemxi)=B1tool;
                  int_li8=0;
                              for posicaoemyi=1:1:divisoesdeyi
                              yfrict=posicaoemyi/divisoesdeyi*W/2;
                              Ri=sqrt((x-xfrict)^2+yfrict^2+zperm2^2);
                              int_li8(posicaoemyi)=1/Ri*(W/2)/divisoesdeyi;
                              end
                              integralfriction_tooly=sum(int_li8)*2;
                  int_li9(posicaoemxi)=Btoolinduced*integralfriction_tooly*lc/divisoesdexi;
            end
                    integralconduction_rake_tool=sum(int_li9);
             paracalculodeq_rake=1/(pi*lambda_t)*integralconduction_rake_tool;
 AUXparacalculodeq_rake_tool(posicaoemx)=paracalculodeq_rake;
end
somatorioparacalculodeq_rake_tool=sum(AUXparacalculodeq_rake_tool);
%
q_rake_induction=somatorioTshearchip/somatorioparacalculodeq_rake_tool;
%%%%%Tfriction na TOOL
for posicaoemz=1:1:divisoesdez
      z=tc*posicaoemz/divisoesdez; %arbitrário.. vai até onde quisermos ver resultados
      simulation=posicaoemz
for posicaoemx=1:1:divisoesdex
x=lc-posicaoemx/divisoesdex*lc;
            for posicaoemxi=1:1:divisoesdexi
              xfrict=posicaoemxi/divisoesdexi*lc;
         %%%%% Sticking and Sliding
                     if xfrict<=lc-lp
                     Vchipss=Vchip;
                     tf1=frictcoef_local*P0*(xfrict/(lc-lp))^xi;
                     else
                     Vchipss=Vchip*(1-(xfrict-(lc-lp))/lp)^2;
                     tf1=frictcoef_local*P0;
                     end
        %%%%%%%%%%%%%%%%%
                  q_friction=tf1*Vchipss;
                  AUXqftool( posicaoemxi)=q_friction;
                  qfteste2=mean(AUXqftool);
                  B1tool=(Btool+difB1)-2*difB1*((lc-xfrict)/lc)^m1-C1*difB1*((lc-xfrict)/lc)^k1;%A/F
                  AUXB1(posicaoemxi)=B1tool;
%                    B1tool=0.1;
                              for posicaoemyi=1:1:divisoesdeyi
                              yfrict=posicaoemyi/divisoesdeyi*W/2;
                              Ri=sqrt((x-xfrict)^2+yfrict^2+z^2);
```

```
                    int_li6(posicaoemyi)=1/Ri*(W/2)/divisoesdeyi;
                    end
                    integralfriction_tooly=sum(int_li6)*2;
               int_li61(posicaoemxi)=q_friction*B1tool*integralfriction_tooly*lc/divisoesdexi;
          end
               integralfriction_tool=sum(int_li61);
 %%%%%%%%%%%%%%%%%%%%%%%
   Tfriction_tool=1/(pi*lambda_t)*integralfriction_tool;
   AUXTfriction_tool(posicaoemx)=Tfriction_tool;
end
AUXMatrizfriction_tool(posicaoemz,:)=AUXTfriction_tool;
%%%%%Tinduction na face RAKE da TOOL
for posicaoemx=1:1:divisoesdex
x=lc-posicaoemx/divisoesdex*lc;
          for posicaoemxi=1:1:divisoesdexi
            xfrict=posicaoemxi/divisoesdexi*lc;
               Btoolinduced=(Bind+difBi)-2*difBi*(xfrict/lc)^mi-Ci*difBi*(xfrict/lc)^ki;
%              B1tool=(Btool+difB1)-2*difB1*(xfrict/lc)^m1-C1*difB1*(xfrict/lc)^k1;
             int_li8=0;
                   for posicaoemyi=1:1:divisoesdeyi
                   yfrict=posicaoemyi/divisoesdeyi*W/2;
                   Ri=sqrt((x-xfrict)^2+yfrict^2+z^2);
                   int_li8(posicaoemyi)=1/Ri*(W/2)/divisoesdeyi;
                   end
                   integralrakeinduction_tooly=sum(int_li8)*2;
             int_li81(posicaoemxi)=Btoolinduced*integralrakeinduction_tooly*lc/divisoesdexi;
          end
               integralfriction_tool=sum(int_li81);
   Tinduction_rake_tool=q_rake_induction/(pi*lambda_t)*integralfriction_tool;
   AUXTinduction_rake_tool(posicaoemx)=Tinduction_rake_tool;
end
AUXMatrizinduction_rake_tool(posicaoemz,:)= AUXTinduction_rake_tool;
end
AUXTtoolsharp=AUXMatrizfriction_tool+AUXMatrizinduction_rake_tool+Tamb;
```

C.6. T tool wear program

```
lambda_t=100;
lf=0.3e-3;
divisoesdexi=100; %divisões de xi
divisoesdeyi=100; %divisões de yi
divisoesdel1=11111;
divisoesdez=100;
%%%%%%%%%%%%%%%%%%%%%%%%%%%%
Bchip=0.77; % Bom balanceamento
difB1=0.21;
m1=0.24;
C1=2;
k1=16;
%%%%%%%%%%%%%%%%%%%%%%%%%%%%
Bind=1; %Valores retirados do trabalho de Komanduri part III
difBi=0.8;
mi=0.3;
Ci=0.2;
ki=4;
%%%%%%%%%%%%%%%%%%%%%%%%%%%%
Bwork=.488;
difB2=0.22;
m2=0.24;
C2=4;
k2=.8;
%%%%%%%%%%%%%%%%%%%%%%%%%%%%
Btool=1-Bchip;
F_Ts=R*sin(-phi+theta); %Eq. (3.31)
Pw=F_Ts*3/(W*lf); %Eq. (3.30)
%b=l3*(1-frictcoef2);
%lfc=lf*(1-lambda);
lfc=lf*(1-sqrt(1/(1+pi/2))); %Eq. (3.33)
%%%%%%%%%%%%%%%%%%%%%%%%%%%%
%%% q induction na face RAKE da TOOL
%Para o lado da chip:
fi=phi-alpha;
V=Vchip;
int_li2=0;
for posicaoemx=1:1:divisoesdex
zperm1=tc; %A posição de z neste cálculo é permanentemente tc.
x=l*sin(fi)-lc*posicaodex/divisoesdex; %Da ponta da ferramenta até ao final do contacto f/a
   for posicaoeml1=1:1:divisoesdel1
                    R21=sqrt((x-l*posicaoeml1/divisoesdel1*sin(fi))^2+(zperm1-
l*posicaoeml1/divisoesdel1*cos(fi))^2)*V/(2*ac);
                    R22=sqrt((x-
l*posicaoeml1/divisoesdel1*sin(fi))^2+(zperm1+l*posicaoeml1/divisoesdel1*cos(fi))^2)*V/(2*ac);
                    if R21==0
                    int_li2(posicaoeml1)=mean(int_li2);
                     AUXsinal(posicaoeml1)=posicaoeml1;
                    else
                    bess21=besselk(0,R21);
```

```
                        bess22=besselk(0,R22);
%                          bess32=0;
                        int_li2(posicaoeml1)=exp(-1*(x-
l*posicaoeml1/divisoesdel1*sin(fi))*V/(2*ac))*(bess21+bess22)*l/divisoesdel1;
                        end
   end
                                           integralshear=sum(int_li2);
  Tshear_chip=(q_shear/(2*pi*lambda_c))*integralshear;
  AUXTshear_chip(posicaoemx)=Tshear_chip;
end
somatorioTshearchip=sum(AUXTshear_chip);
%
for posicaoemx=1:1:divisoesdex
x=posicaoemx/divisoesdex*lc; %Do final do contacto f/a até à ponta da ferramenta.
zperm2=0;  %A posição de z neste cálculo é permanentemente zero.
             for posicaoemxi=1:1:divisoesdexi
               xfrict=posicaoemxi/divisoesdexi*lc;
                       Btoolinduced=(Bind+difBi)-2*difBi*(xfrict/lc)^mi-Ci*difBi*(xfrict/lc)^ki;
%                      B1tool=(Btool+difB1)-2*difB1*(xfrict/lc)^m1-C1*difB1*(xfrict/lc)^k1;
                    int_li8=0;
                                 for posicaoemyi=1:1:divisoesdeyi
                                 yfrict=posicaoemyi/divisoesdeyi*W/2;
                                 Ri=sqrt((x-xfrict)^2+yfrict^2+zperm2^2);
                                 int_li8(posicaoemyi)=1/Ri*(W/2)/divisoesdeyi;
                                 end
                                 integralfriction_tooly=sum(int_li8)*2;
                    int_li9(posicaoemxi)=Btoolinduced*integralfriction_tooly*lc/divisoesdexi;
             end
                      integralconduction_rake_tool=sum(int_li9);
              paracalculodeq_rake=1/(pi*lambda_t)*integralconduction_rake_tool;
 AUXparacalculodeq_rake_tool(posicaoemx)=paracalculodeq_rake;
end
somatorioparacalculodeq_rake_tool=sum(AUXparacalculodeq_rake_tool);
%
q_rake_induction=somatorioTshearchip/somatorioparacalculodeq_rake_tool;
%%% q induction na face FLANK da TOOL
for posicaoemx=1:1:divisoesdex
   fi=pi/2-phi;
z=l*cos(fi);
x=-l*sin(fi)-lf*posicaodex/divisoesdex;
%
   for posicaoeml1=1:1:divisoesdel1
                        R31=sqrt((x+l*posicaoeml1/divisoesdel1*sin(fi))^2+(z-
l*posicaoeml1/divisoesdel1*cos(fi))^2)*V/(2*ac);

R32=sqrt((x+l*posicaoeml1/divisoesdel1*sin(fi))^2+(z+l*posicaoeml1/divisoesdel1*cos(fi))^2)*V/(2
*ac);
                        if R31==0
                        int_li3(posicaoeml1)=mean(int_li3);
                         AUXsinal(posicaoeml1)=posicaoeml1;
                        else
                        bess31=besselk(0,R31);
                        bess32=besselk(0,R32);
%                          bess32=0;
```

```
                        int_li3(posicaoeml1)=exp(-
1*(x+l*posicaoeml1/divisoesdel1*sin(fi))*V/(2*ac))*(bess31+bess32)*l/divisoesdel1;
                        end
    end
                                            integralshear=sum(int_li3);
                        %
   Tshear_work=(q_shear/(2*pi*lambda_c))*integralshear;
   AUXTshear_work(posicaoemx)=Tshear_work;
end
somatorioTshearwork=sum(AUXTshear_work);
%
for posicaoemx=1:1:divisoesdex
    zperm=0;  %A posição de z neste cálculo é permanentemente zero.
x=posicaoemx/divisoesdex*lf;
               for posicaoemxi=1:1:divisoesdexi
                  xfriction=posicaoemxi/divisoesdexi*lf;
                      Btoolinduced=(Bind+difBi)-2*difBi*(xfriction/lf)^mi-Ci*difBi*(xfriction/lf)^ki;
%                     B2work=(Bwork-difB2)+2*difB2*(xfriction/lf)^m2+C2*difB2*(xfriction/lf)^k2;
                                   for posicaoemyi=1:1:divisoesdeyi
                                   yfrict=posicaoemyi/divisoesdeyi*W/2;
                                   Ri=sqrt((x-xfriction)^2+yfrict^2+zperm^2);
                                   int_li9(posicaoemyi)=1/Ri*(W/2)/divisoesdeyi;
                                   end
                                   integral_tooly=sum(int_li9)*2;
                         int_li91(posicaoemxi)=(1-Btoolinduced)*integral_tooly*lf/divisoesdexi;
               end
                         integralconduction_flank_tool=sum(int_li91);
                paracalculodeq_flank=1/(pi*lambda_t)*integralconduction_flank_tool;
 AUXparacalculodeq_flank_tool(posicaoemx)=paracalculodeq_flank;
end
somatorioparacalculodeq_flank_tool=sum(AUXparacalculodeq_flank_tool);
%
q_flank_induction=somatorioTshearwork/somatorioparacalculodeq_flank_tool;
for posicaoemz=1:1:divisoesdez
        varz=posicaoemz/divisoesdez; %arbitrário.. vai até onde quisermos ver resultados
        simulation=posicaoemz
%%%%%Tfriction na TOOL
for posicaoemx=1:1:divisoesdex
    z=(lf*cos (alpha))*varz;
    x=lc-lc*posicaoemx/divisoesdex-(lf*sin (alpha))*varz;
% x=lc-posicaoemx/divisoesdex*lc;
               for posicaoemxi=1:1:divisoesdexi
                  xfrict=posicaoemxi/divisoesdexi*lc;
            %%%%% Sticking and Sliding
                         if xfrict<=lc-lp
                         Vchipss=Vchip;
                         tf1=frictcoef_local*P0*(xfrict/(lc-lp))^xi;
                         else
                         Vchipss=Vchip*(1-(xfrict-(lc-lp))/lp)^2;
                         tf1=frictcoef_local*P0;
                         end
           %%%%%%%%%%%%%%%%%%
                       q_friction=tf1*Vchipss;
                       AUXqftool( posicaoemxi)=q_friction;
```

```
            qfteste2=mean(AUXqftool);
            B1tool=(Btool+difB1)-2*difB1*((lc-xfrict)/lc)^m1-C1*difB1*((lc-xfrict)/lc)^k1;%A/F
            AUXB1(posicaoemxi)=B1tool;
%             B1tool=0.1;
                    for posicaoemyi=1:1:divisoesdeyi
                    yfrict=posicaoemyi/divisoesdeyi*W/2;
                    Ri=sqrt((x-xfrict)^2+yfrict^2+z^2);
                    int_li6(posicaoemyi)=1/Ri*(W/2)/divisoesdeyi;
                    end
                    integralfriction_tooly=sum(int_li6)*2;
             int_li61(posicaoemxi)=q_friction*B1tool*integralfriction_tooly*lc/divisoesdexi;
        end
             integralfriction_tool=sum(int_li61);
 %%%%%%%%%%%%%%%%%%%%%
  Tfriction_tool=1/(pi*lambda_t)*integralfriction_tool;
  AUXTfriction_tool(posicaoemx)=Tfriction_tool;
end
AUXMatrizfriction_tool(posicaoemz,:)=AUXTfriction_tool;
%%%%%Tinduction na face RAKE da TOOL
for posicaoemx=1:1:divisoesdex
    z=(lf*cos (alpha))*varz;
    x=lc-lc*posicaoemx/divisoesdex-(lf*sin (alpha))*varz;
% x=lc-posicaoemx/divisoesdex*lc;
        for posicaoemxi=1:1:divisoesdexi
         xfrict=posicaoemxi/divisoesdexi*lc;
              Btoolinduced=(Bind+difBi)-2*difBi*(xfrict/lc)^mi-Ci*difBi*(xfrict/lc)^ki;
%             B1tool=(Btool+difB1)-2*difB1*(xfrict/lc)^m1-C1*difB1*(xfrict/lc)^k1;
            int_li8=0;
                   for posicaoemyi=1:1:divisoesdeyi
                   yfrict=posicaoemyi/divisoesdeyi*W/2;
                   Ri=sqrt((x-xfrict)^2+yfrict^2+z^2);
                   int_li8(posicaoemyi)=1/Ri*(W/2)/divisoesdeyi;
                   end
                   integralrakeinduction_tooly=sum(int_li8)*2;
            int_li81(posicaoemxi)=Btoolinduced*integralrakeinduction_tooly*lc/divisoesdexi;
        end
             integralfriction_tool=sum(int_li81);
  Tinduction_rake_tool=q_rake_induction/(pi*lambda_t)*integralfriction_tool;
  AUXTinduction_rake_tool(posicaoemx)=Tinduction_rake_tool;
end
AUXMatrizinduction_rake_tool(posicaoemz,:)=AUXTinduction_rake_tool;
%%%%%Trubbing na TOOL
for posicaoemx=1:1:divisoesdex
  z=(lc*cos (alpha))*varz;
  x=lf-lf*posicaoemx/divisoesdex-(lc*sin (alpha))*varz;
        for posicaoemxi=1:1:divisoesdexi
        xrubbing=posicaoemxi/divisoesdexi*lf;
      %%%%% variaçao na zona do rubbing
            if xrubbing<=lf-lfc
%             tf2=frictcoef2*P2*(xrubbing/(l3-b))^xi;
          tf3=lambda*Pw*(xrubbing/(lf-lfc))^xi;
            tf23(posicaoemxi)=tf3;
            else
%             tf2=tens_s;
          tf3=lambda*Pw;
```

```
                  tf23(posicaoemxi)=tf3;
                  end
                  q_rubbing=tf3*Vc;
                  B2work=(Bwork-difB2)+2*difB2*(xrubbing/lf)^m1+C2*difB2*(xrubbing/lf)^k2;
         %%%%%%
                  int_li7=0;
                            for posicaoemyi=1:1:divisoesdeyi
                            yfrict=posicaoemyi/divisoesdeyi*W/2;
                            Ri=sqrt((x-xrubbing)^2+yfrict^2+z^2);
                            int_li7(posicaoemyi)=1/Ri*(W/2)/divisoesdeyi;
                            end
                            integralrubbing_tooly=sum(int_li7)*2;
                    int_li71(posicaoemxi)=q_rubbing*(1-
B2work)*integralrubbing_tooly*lf/divisoesdexi;
            end
                    integralrubbing_tool=sum(int_li71);
             Trubbing_tool=1/(pi*lambda_t)*integralrubbing_tool;
 AUXTrubbing_tool(posicaoemx)=Trubbing_tool;
end
AUXMatrizrubbing_tool(posicaoemz,:)=AUXTrubbing_tool;
%%%%%%%%%%%%%%%%%%%%%%%%%%
%%%%%Tinduction na face FLANK da TOOL
for posicaoemx=1:1:divisoesdex
      z=(lc*cos (alpha))*varz;
      x=lf-lf*posicaoemx/divisoesdex-(lc*sin (alpha))*varz;
            for posicaoemxi=1:1:divisoesdexi
              xfriction=posicaoemxi/divisoesdexi*lf;
                 Btoolinduced=(Bind+difBi)-2*difBi*(xfriction/lf)^mi-Ci*difBi*(xfriction/lf)^ki;
%                B2work=(Bwork-difB2)+2*difB2*(xfriction/lf)^m2+C2*difB2*(xfriction/lf)^k2;
                            for posicaoemyi=1:1:divisoesdeyi
                            yfrict=posicaoemyi/divisoesdeyi*W/2;
                            Ri=sqrt((x-xfriction)^2+yfrict^2+z^2);
                            int_li9(posicaoemyi)=1/Ri*(W/2)/divisoesdeyi;
                            end
                            integral_tooly=sum(int_li9)*2;
                    int_li91(posicaoemxi)=(1-Btoolinduced)*integral_tooly*lf/divisoesdexi;
            end
                    integralconduction_flank_tool=sum(int_li91);
             Tinduction_flank_tool=q_flank_induction/(pi*lambda_t)*integralconduction_flank_tool;
 AUXTinduction_flank_tool(posicaoemx)=Tinduction_flank_tool;
end
AUXMatrizinduction_flank_tool(posicaoemz,:)= AUXTinduction_flank_tool;
end
AUXMatrizTtoolwear=AUXMatrizfriction_tool+AUXMatrizrubbing_tool+AUXMatrizinduction_rak
e_tool+AUXMatrizinduction_flank_tool+Tamb;
```

C.7. T work program

```
lambda_t=100;
lf=0.3e-3;
divisoesdexi=100; %divisões de xi
divisoesdeyi=100; %divisões de yi
divisoesdel1=1111;
divisoesdazonaderubbing=1111;
%%%%%%%%%%%%%%%%%%%%%%%%%
Bchip=0.77; % Bom balanceamento
difB1=0.21;
m1=0.24;
C1=2;
k1=16;
%%%%%%%%%%%%%%%%%%%%%%%%%
Bind=1; %Valores retirados do trabalho de Komanduri part III
difBi=0.8;
mi=0.3;
Ci=0.2;
ki=4;
%%%%%%%%%%%%%%%%%%%%%%%%%
Bwork=.488;
difB2=0.22;
m2=0.24;
C2=4;
k2=.8;
%%%%%%%%%%%%%%%%%%%%%%%%%
Btool=1-Bchip;
F_Ts=R*sin(-phi+theta); %Eq. (3.31)
Pw=F_Ts*3/(W*lf); %Eq. (3.30)
lfc=lf*(1-sqrt(1/(1+pi/2))); %Eq. (3.33)
%%%%%%%%%%%%%%%%%%%%%%%%%
%%% q induction na face RAKE da TOOL
%Para o lado da chip:
fi=phi-alpha;
V=Vchip;
int_li2=0;
int_li3=0;
int_li5=0;
%Tshear workpiece
%Para o lado da Workpiece:
fi=pi/2-phi;
V=Vc;
for posicaoemz=1:1:divisoesdez
        varz=posicaoemz/divisoesdez; %arbitrário.. vai até onde quisermos ver resultados
        simulation=posicaoemz
for posicaodex=1:1:divisoesdex
z=l*cos(fi)+l/4*varz; %área por baixo da flank face com comprimento l (1)
x=-l*sin(fi)-lf*posicaodex/divisoesdex; %Da ponta da ferramenta para o final de l3 (1)
    for posicaoeml1=1:1:divisoesdel1
                         R31=sqrt((x+l*posicaoeml1/divisoesdel1*sin(fi))^2+(z-
l*posicaoeml1/divisoesdel1*cos(fi))^2)*V/(2*ac);
```

```
R32=sqrt((x+l*posicaoeml1/divisoesdel1*sin(fi))^2+(z+l*posicaoeml1/divisoesdel1*cos(fi))^2)*V/(2
*ac);
                    if R31==0
                    int_li3(posicaoeml1)=mean(int_li3);
                     AUXsinal(posicaoeml1)=posicaoeml1;
                    else
                    bess31=besselk(0,R31);
                    bess32=besselk(0,R32);
%                       bess32=0;
                    int_li3(posicaoeml1)=exp(-
1*(x+l*posicaoeml1/divisoesdel1*sin(fi))*V/(2*ac))*(bess31+bess32)*l/divisoesdel1;
                    end
   end
                                    integralshear=sum(int_li3);
  AUXint(posicaodex)=integralshear;
  Tshear_workpiece=(q_shear/(2*pi*lambda_c))*integralshear;
  AUXTshear_workpiece(posicaodex)=Tshear_workpiece;
end
AUXMatrizshear_work(posicaoemz,:)=AUXTshear_workpiece;
%%%%%Trubbing workpiece
for posicaodex=1:1:divisoesdex
z=l/4*varz; % (1)
x=lf-lf*posicaodex/divisoesdex; % (1)
int_li5=0;
for posicaonazonaderubbing=1:1:divisoesdazonaderubbing
             xrubbing=posicaonazonaderubbing/divisoesdazonaderubbing*lf;
        %%%%% rubbing
          if xrubbing<=lf-lfc
             tf2=lambda*Pw*(xrubbing/(lf-lfc))^xi;
            tf22(posicaonazonaderubbing)=tf2;
          else
             tf2=lambda*Pw;
             tf22(posicaonazonaderubbing)=tf2;
          end
                q_rubbing=tf2*Vc;
                B2work=(Bwork-difB2)+2*difB2*(xrubbing/lf)^m2+C2*difB2*(xrubbing/lf)^k2;
                   R51=sqrt((x-xrubbing)^2+(z)^2)*Vc/(2*ac);
                    if R51==0
                    int_li5(posicaonazonaderubbing)=0;
                    else
                    bess51=besselk(0,R51);
                    int_li5(posicaonazonaderubbing)=q_rubbing*B2work*exp(-1*(x-
lf*posicaonazonaderubbing/divisoesdazonaderubbing)*(Vc/(2*ac)))*(bess51)*lf/divisoesdazonaderub
bing;
                    end
end
                                          integralrubbing_work=sum(int_li5);
  Trubbing_work=1/(pi*lambda_c)*integralrubbing_work;
  AUXTrubbing_work(posicaodex)=Trubbing_work;
end
AUXMatrizrubbing_work(posicaoemz,:)=AUXTrubbing_work;
end
AUXMatrizTworkpiece=AUXMatrizrubbing_work+AUXMatrizshear_work+Tamb;
```